Article

Developmental Cell

Seipin Facilitates Triglyceride Flow to Lipid Droplet and Counteracts Droplet Ripening via Endoplasmic Reticulum Contact

Graphical Abstract

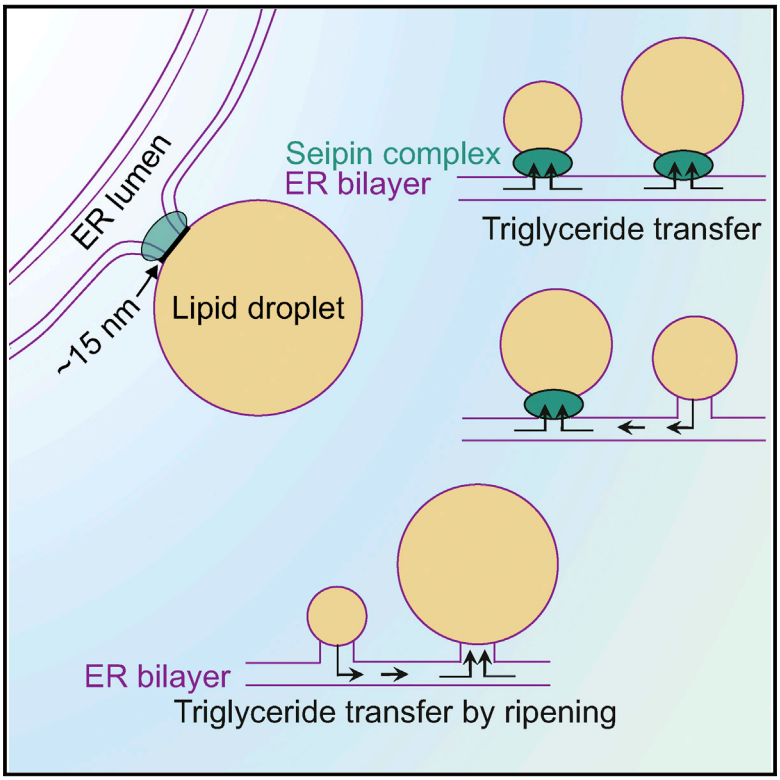

Authors

Veijo T. Salo, Shiqian Li, Helena Vihinen, ..., Abdou Rachid Thiam, Eija Jokitalo, Elina Ikonen

Correspondence

thiam@ens.fr (A.R.T.), eija.jokitalo@helsinki.fi (E.J.), elina.ikonen@helsinki.fi (E.I.)

In Brief

Salo et al. show that seipin determines where a lipid droplet (LD) forms and establishes a neck between ER and LD. LDs continuously exchange lipids via ER, and biophysically, larger LDs acquire lipids more readily than smaller ones. Seipin facilitates lipid transfer to droplets, helping small LDs to grow.

Highlights

- Seipin can determine the site of LD formation
- Seipin-mediated ER-LD membrane contacts display a uniform neck-like architecture
- Seipin at ER-LD contact facilitates continuous triglyceride transfer to LD
- Acute removal of seipin reveals a principle of LD ripening via the ER

Salo et al., 2019, Developmental Cell *50*, 1–16
August 19, 2019
https://doi.org/10.1016/j.devcel.2019.05.016

CellPress

Please cite this article in press as: Salo et al., Seipin Facilitates Triglyceride Flow to Lipid Droplet and Counteracts Droplet Ripening via Endoplasmic Reticulum Contact, Developmental Cell (2019), https://doi.org/10.1016/j.devcel.2019.05.016

Developmental Cell
Article

Seipin Facilitates Triglyceride Flow to Lipid Droplet and Counteracts Droplet Ripening via Endoplasmic Reticulum Contact

Veijo T. Salo,[1,2,8] Shiqian Li,[1,2,8] Helena Vihinen,[3] Maarit Hölttä-Vuori,[1,2] Abel Szkalisity,[4] Peter Horvath,[4] Ilya Belevich,[3] Johan Peränen,[1,2] Christoph Thiele,[5] Pentti Somerharju,[6] Hongxia Zhao,[3] Alexandre Santinho,[7] Abdou Rachid Thiam,[7,9,*] Eija Jokitalo,[3,9,*] and Elina Ikonen[1,2,9,10,*]

[1]Department of Anatomy, Faculty of Medicine, University of Helsinki, Helsinki, Finland
[2]Minerva Foundation Institute for Medical Research, Helsinki, Finland
[3]Institute of Biotechnology, University of Helsinki, Helsinki, Finland
[4]Biological Research Center, Szeged, Hungary
[5]Limes Institute, University of Bonn, Bonn, Germany
[6]Department of Biochemistry, Faculty of Medicine, University of Helsinki, Helsinki, Finland
[7]Laboratoire de Physique de l'Ecole Normale Supérieure, ENS, Université PSL, CNRS, Sorbonne Université, Universite de Paris, Paris, France
[8]These authors contributed equally
[9]Senior author
[10]Lead Contact
*Correspondence: thiam@ens.fr (A.R.T.), eija.jokitalo@helsinki.fi (E.J.), elina.ikonen@helsinki.fi (E.I.)
https://doi.org/10.1016/j.devcel.2019.05.016

SUMMARY

Seipin is an oligomeric integral endoplasmic reticulum (ER) protein involved in lipid droplet (LD) biogenesis. To study the role of seipin in LD formation, we relocalized it to the nuclear envelope and found that LDs formed at these new seipin-defined sites. The sites were characterized by uniform seipin-mediated ER-LD necks. At low seipin content, LDs only grew at seipin sites, and tiny, growth-incompetent LDs appeared in a Rab18-dependent manner. When seipin was removed from ER-LD contacts within 1 h, no lipid metabolic defects were observed, but LDs became heterogeneous in size. Studies in seipin-ablated cells and model membranes revealed that this heterogeneity arises via a biophysical ripening process, with triglycerides partitioning from smaller to larger LDs through droplet-bilayer contacts. These results suggest that seipin supports the formation of structurally uniform ER-LD contacts and facilitates the delivery of triglycerides from ER to LDs. This counteracts ripening-induced shrinkage of small LDs.

INTRODUCTION

Lipid droplets (LDs) are storage organelles consisting of a core of neutral lipids surrounded by a phospholipid monolayer (Pol et al., 2014; Welte, 2015) and are dynamically remodeled in response to altered metabolic status (Herms et al., 2015; Rambold et al., 2015). LD biogenesis begins in the endoplasmic reticulum (ER), which harbors triglyceride-synthesizing diacylglycerol acyltransferase (DGAT) enzymes (Walther et al., 2017). It is postulated that newly synthesized neutral lipids first diffuse in the bilayer but, with rising local concentration, spontaneously aggregate and form nm-sized lenses. Such structures have been reported in yeast (Choudhary et al., 2015), but it is unclear how they transform into the observed >100- to 200-nm-diameter nascent LDs (Kassan et al., 2013; Salo et al., 2016; Wang et al., 2016).

A nascent LD can further grow both by local neutral lipid synthesis on the LD monolayer and via lipid transfer from the ER. In yeast and several mammalian cell types, LDs appear to retain a functional connectivity with the ER (Jacquier et al., 2011; Salo et al., 2016; Wilfling et al., 2013). Considering the mounting evidence for membrane continuities between the ER and LDs, there are likely machineries that control these contacts and regulate LD growth (Ohsaki et al., 2017; Salo and Ikonen, 2019; Schuldiner and Bohnert, 2017). Seipin, a homo-oligomeric ER transmembrane protein that localizes to ER-LD contacts, may be part of such machinery (Binns et al., 2010; Fei et al., 2008; Salo et al., 2016; Szymanski et al., 2007; Wang et al., 2016).

Seipin was identified as the gene defective in BSCL2, the most severe lipodystrophy in man (Magré et al., 2001). Studies in multiple model systems have implicated seipin to be crucial for normal LD formation and adipogenesis (Boutet et al., 2009; Cai et al., 2015; Cui et al., 2011; Fei et al., 2008; Szymanski et al., 2007; Tian et al., 2011). Seipin may facilitate the growth of LDs (Salo et al., 2016; Wang et al., 2016), with suggested functions in regulating the enzyme machinery of *de novo* lipogenesis or phosphatidic acid metabolism (Cartwright et al., 2015; Fei et al., 2011; Pagac et al., 2016; Talukder et al., 2015; Wolinski et al., 2015), acting as a diffusion barrier for proteins between the ER and LDs (Grippa et al., 2015), regulating lipolysis (Chen et al., 2012), or controlling Ca^{2+} metabolism (Bi et al., 2014). Remarkably, seipin deficiency consistently results in the accumulation of tiny and supersized LDs, but the origin of this LD size heterogeneity remains elusive.

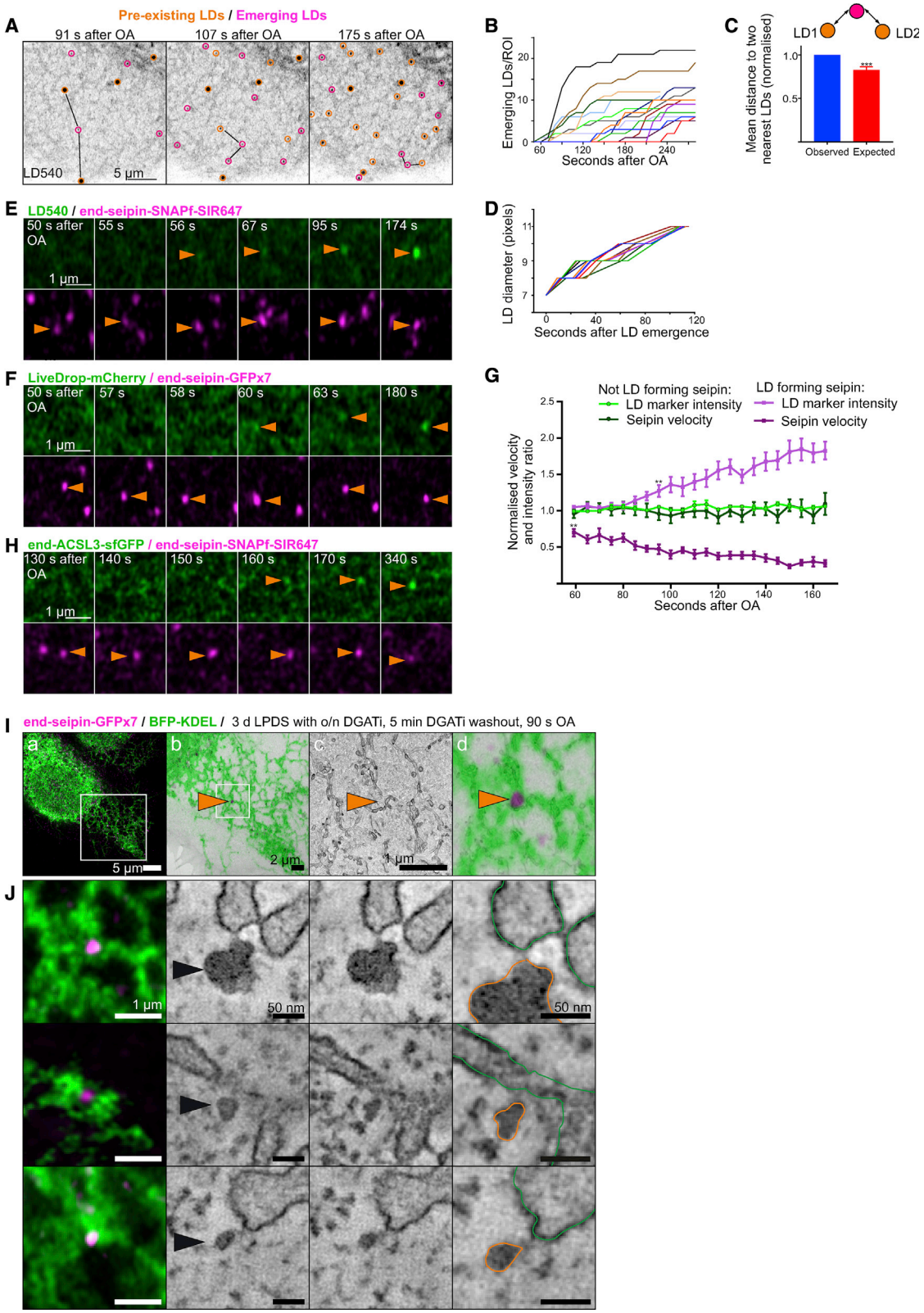

Figure 1. Seipin at LD Formation Sites

(A) Cells with seipin tagged endogenously with SNAPf were delipidated for 3 days and imaged by Airyscan microscopy, starting 50 s after OA loading. Orange circles, pre-existing LDs; magenta circles, LDs forming between time points.

(legend continued on next page)

From a biophysical standpoint, LDs are oil-in-water emulsion droplets expected to undergo well-known spontaneous destabilization processes (Thiam et al., 2013). Droplets are thermodynamically unstable because the interface between the immiscible fluids is unfavorable and generates surface tension. Therefore, droplets tend to mix their contents to minimize the interface (Penno et al., 2013). This can be achieved by two mechanisms: fusion, which is a rapid merging or coalescence of droplets, or Ostwald ripening, a molecular diffusion process by which smaller droplets continuously leak material to bigger ones through a connecting phase (Thiam and Forêt, 2016; Thiam et al., 2013). Ripening happens in this direction because of the higher internal pressure of smaller droplets, imposing a flux of molecules toward lower pressure, i.e., bigger droplets (Thiam and Forêt, 2016; Thiam et al., 2013). Both droplet fusion and ripening would lead to the formation of supersized droplets (Thiam and Beller, 2017). Whether seipin controls these processes to regulate LDs is so far unknown.

Here, we report that seipin can determine the site of LD formation, that <100 nm diameter LDs emerge from the ER, and that seipin-mediated ER-LD contacts display a uniform membrane architecture. Using rapid depletion of seipin from pre-existing ER-LD contacts and model membrane studies, we provide evidence that seipin facilitates continuous delivery of triglycerides from the ER to LDs, and thereby counterbalances ripening.

RESULTS

LD Formation at Seipin-Defined Sites

Here, we employed human A431 cells to study the basic mechanisms of LD formation and maintenance, focusing on the role of seipin. These cells are well suited for genetic engineering and imaging and have been used for studying lipogenesis and LD formation (Moessinger et al., 2011; Poppelreuther et al., 2018). In these cells, endogenously tagged seipin exists as discrete ER-resident complexes that move along the ER (Salo et al., 2016). During LD biogenesis, a subset of seipin complexes (termed here seipins) becomes stably associated with ER-LD contacts, with reduced motility and with virtually all LDs harboring seipin at later time points (Salo et al., 2016; Wang et al., 2016). To investigate when seipin gets stabilized at ER-LD contacts, we performed live-cell imaging during the first minutes of LD biogenesis induced by oleic acid (OA) addition. We engineered cell lines with seipin tagged endogenously with either a fast labeling variant of the self-labeling SNAP-tag (SNAPf) (Sun et al., 2011) or split 7xGFP (Kamiyama et al., 2016) (Figures S1A and S1B) and used the bright lipophilic dye LD540 (Spandl et al., 2009) or the model peptide LiveDrop-mCherry (Wang et al., 2016) as markers for forming LDs. This revealed that the timing of LD formation and the number of forming LDs varied from cell to cell, but typically, newly forming droplets became visible at ~60 s after OA addition (Figures 1A and 1B). They emerged at spatially dispersed sites throughout the ER, in agreement with (Kassan et al., 2013). Moreover, the minimal distance between neighboring forming droplets was higher than expected by random simulation (Figures 1C and S1C), suggesting that LD nucleation is non-stochastic. After appearance, LDs grew at a roughly similar rate (Figure 1D).

When tracking seipins that became associated with ER-LD contacts, we found seipin motility to be decreased prior to the accumulation of LD540, LiveDrop-mCherry or endogenously tagged ACSL3, the major acyl-CoA synthetase ligase in these cells (Poppelreuther et al., 2018), proposed to mark LD formation sites (Kassan et al., 2013) (Figures 1E–1H and S1D–S1F). We then took advantage of the early stabilization of seipin at LD-forming sites to investigate these structures by correlative light electron microscopy (CLEM). Furthermore, as partial seipin depletion enriched the fraction of seipins engaged in LD formation without evident changes in LD protein recruitment (Figures S1G and S1H), we focused on seipin knockdown cells. Cells were first stringently delipidated (3 days in lipoprotein-deficient-serum medium, LPDS, including overnight with DGAT1 and DGAT2 inhibitors, followed by a 5-min inhibitor washout) and then treated with OA for 90 s. Fluorescent ER marker was employed to correlate light and electron microscopy (EM) images and to identify the localization of seipins in tomograms (Figure 1I). Using this strategy, half of the seipin sites examined revealed very small LD-like structures that ranged from ~30 to ~100 nm in diameter (65 ± 25 nm, mean ± SD, n = 7 droplets). These putative nascent LDs exhibited an electron dense core and a thin thread-like bridge to the nearby ER (Figure 1J). Overall, these data suggest that in A431 cells, the first LDs appear relatively synchronously but spatially separated from each other, that seipin is present at early stages of LD formation, and that

(B) Analysis of (A). n = 16 cells, 4 experiments.
(C) Distances of newly formed LDs to two nearest neighboring LDs were measured and compared with simulated images. Bars: mean ± SEM, n = 15 cells, 4 experiments. ***p < 0.0005 (Mann-Whitney test).
(D) Growth rate of individual LDs, pixel size 34.5 nm.
(E) Insets of video in (A). Orange arrowheads, immobilized SNAPf-seipin and subsequent LD540 accumulation at nascent LD.
(F) End-seipin-GFPx7 cells stably expressing BFP-KDEL (not shown) and LiveDrop-mCherry were delipidated for 1 day and imaged after OA loading. Orange arrowheads, immobilized seipin and subsequent LiveDrop accumulation at nascent LD.
(G) Analysis of (F). Tracking of LD-forming and not LD-forming seipins upon OA addition. Motility of seipins and LiveDrop/KDEL intensity ratio at seipin foci, ± SEM, n = 15–20 seipins from 6 cells, 3 experiments. **p < 0.005 (unpaired t test).
(H) Cells with sfGFP engineered to endogenous ACSL3 locus and SNAPf to endogenous seipin locus were delipidated for 3 days and imaged after OA loading. Orange arrowheads, immobilized seipin and subsequent ACSL3 accumulation at nascent LDs.
(I) End-seipin-GFPx7 cells expressing BPF-KDEL and partially seipin depleted by siRNAs or lentiviruses were treated as indicated, fixed, imaged by Airyscan microscopy (a and b), and processed for EM. Fluorescence and TEM images were correlated (b) and sections subjected to tomography. Minimum intensity projection image was generated from tomograms (c) and overlaid with fluorescent images to pinpoint the seipin-defined site (d).
(J) Examples of seipin and ER from Airyscan images as in (I) and tomogram slices from corresponding areas. Black arrowheads indicate LDs, green outlines ER, and orange outlines nascent LDs.
See also Figure S1.

Please cite this article in press as: Salo et al., Seipin Facilitates Triglyceride Flow to Lipid Droplet and Counteracts Droplet Ripening via Endoplasmic Reticulum Contact, Developmental Cell (2019), https://doi.org/10.1016/j.devcel.2019.05.016

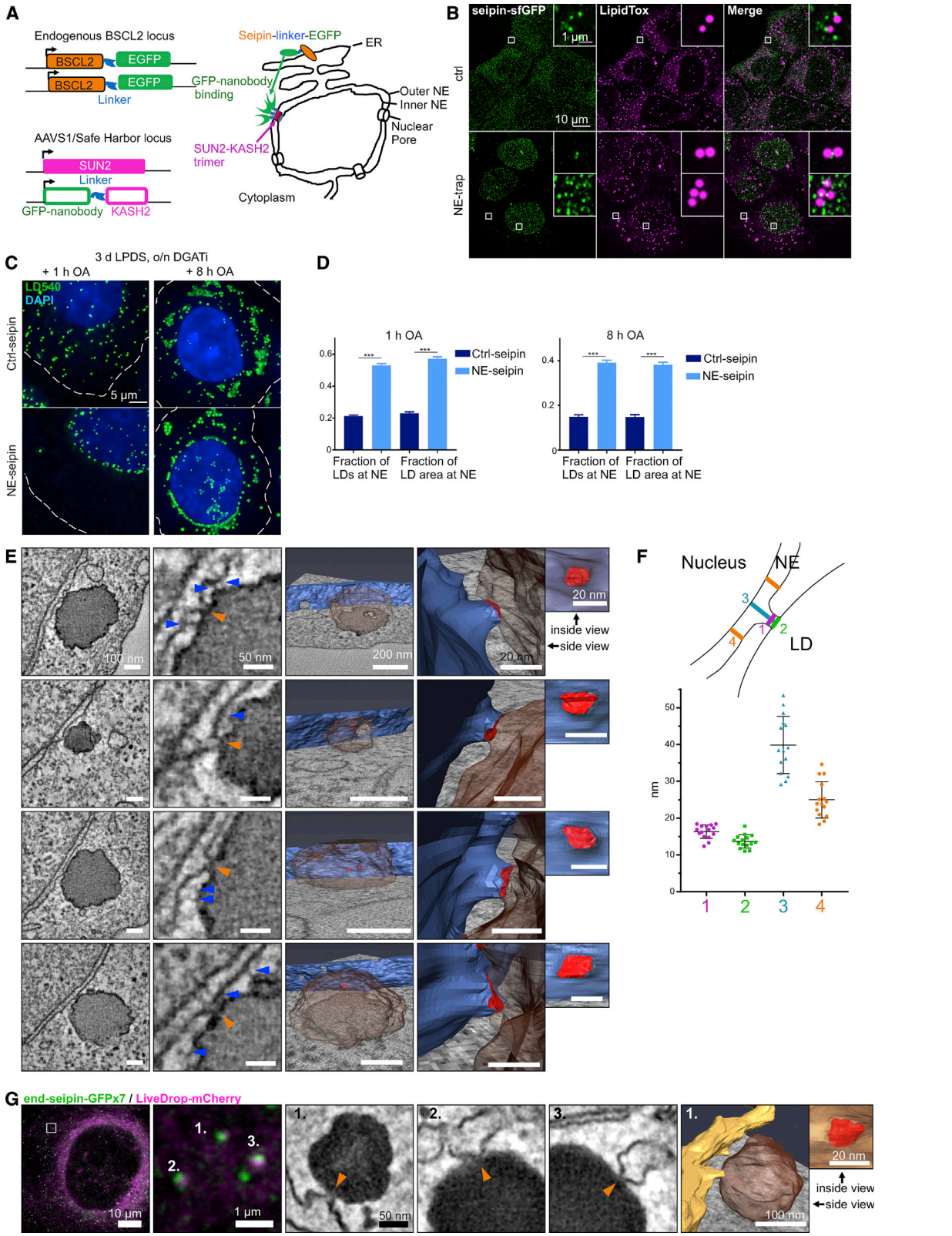

(legend on next page)

droplet-like structures with a diameter of ~30 nm can be found at seipin-defined sites.

Redistribution of Seipin in the ER Relocalizes LD Biogenesis

Since seipin was present at early stages during LD assembly, we wondered whether seipin could contribute to spatially defining a subdomain of the ER that is destined for LD formation. To test this idea, we used a GFP-nanobody-based system to trap endogenously tagged seipin-GFP at a well-defined ER subdomain, the nuclear envelope (NE). In this system, the GFP nanobody (Rothbauer et al., 2006) is fused to a KASH2 fragment that binds SUN2 at the NE (Sosa et al., 2012). Seipin-GFP that reaches the nanobody is thus trapped at the cytoplasmic face of the NE (Figure 2A). Upon transient transfection of this system into cells with endogenously tagged seipin-GFP, we found newly formed LDs to be enriched at the NE (Figure 2B). To facilitate analysis, we generated stable clones and found that the fraction of LDs localizing to the NE was increased from ~20% in control cells to ~60% in NE-seipin-trapped cells, without any obvious LD growth defect (Figures 2C, 2D, and S1I). The effect was specific, as it was reversed by SUN small interfering RNAs (siRNAs) (Figure S1J). The phenotype also persisted during longer OA incubations (Figures 2C and 2D), and NE-trapped LDs displayed reduced motility (Figure S1K), in line with the idea that seipin-LD contacts are long lasting (Salo et al., 2016). Interestingly, also at the NE, LDs formed at dispersed sites, with the nearest distance between newly forming LDs higher than expected by chance (Figure S1L).

Seipin-Mediated LD Contacts Display a Uniform Neck

The fixed architecture of the NE, as compared to the rest of the ER, enabled us to more accurately investigate the structure of seipin-mediated membrane-LD contacts. To this end, we imaged 1 h LDs from NE-seipin-trapped cells by electron tomography (ET). Most of the LDs had 1–2 clear NE contacts with a strikingly uniform appearance (Figures 2E and 2F, orange arrowheads). The contact consisted of a neck-like protrusion extending from the NE and seemingly fusing with the LD. A small fraction of the LD monolayer appeared to be in direct contact with the ER lumen, with a membrane continuity between the NE and the LD surface. Interestingly, the dimensions of this contact site and the adjacent neck were strikingly regular (Figure 2F). The diameter of the neck at its narrowest point was 16.3 ± 1.9 nm (SD, n = 15), the diameter of the droplet surface potentially in contact with the ER lumen was 13.6 ± 1.8 nm (SD, n = 15), and the overall surface area of the contact approximated from 3D reconstructions was approximately ~250 nm^2. Thin fiber-like connections surrounding the seipin-defined contact and extending between the NE and LDs were also frequently detected (Figure 2E, blue arrowheads). We also investigated contacts between the ER and newly formed LDs in cells without NE trapping of seipin. Using CLEM, we found seipin-positive contact sites of very similar dimensions (Figure 2G). Moreover, similar contacts could also be identified in wild-type (WT) A431 cells and primary human fibroblasts (Figures S2A–S2C). We propose that this morphology represents the general architecture of seipin-mediated ER-LD contacts. Why a similar uniform ER-LD neck was not apparent in the smallest LDs observed is not known, but points to the possibility that there might be more conformational flexibility in this region during the initial stages of budding.

Acute Depletion of Seipin via Auxin-Inducible Degradation

To investigate the function of seipin at pre-existing ER-LD contacts we generated a system in which endogenously GFP-tagged seipin could be acutely depleted from cells by adapting the auxin (indole-3-acetic acid, IAA)-inducible degron (AID) system (Nishimura et al., 2009) (Figure 3A). With this system, auxin-inducible seipin depletion was achieved very rapidly (>95% reduction of seipin protein in 30 min, Figure 3B), while IAA had no effect on control (ctrl) cells, which lacked OsTIR1 expression (Figure 3B). Seipin depletion was accompanied by about 30% constitutive depletion of the protein (in stable seipin degron-A line). In another stable cell line, no basal depletion in the absence of auxin was present, but seipin depletion was somewhat slower (95% degradation in 2 h; seipin degron-B line, Figures S2D–S2F). The results were comparable between the cell lines, and for most experiments, the faster depleting line was employed. Importantly, the depletion was also efficient in lipid-loaded cells, where seipin was degraded from pre-existing ER-LD contacts (Figures 3B and 3C), accompanied by apparent loss of the characteristic neck structure (Figures S2G and S2H).

When such seipin degron cells were first delipidated in the presence of auxin and then loaded with OA for 2 h, an LD phenotype typical for seipin knockout (KO) cells (Salo et al., 2016; Wang et al., 2016) became evident, with accumulation of

Figure 2. Seipin Relocalizes LD Formation and Seipin-LD Contacts Have Uniform Membrane Architecture

(A) Schematic of seipin-NE trap.

(B) End-seipin-sfGFP cells were transfected for 2 days with the NE trap system, treated with OA for 3 h, and fixed for imaging. Airyscan z-stack maximum intensity projections of transfected and non-transfected cells.

(C) Stable cell lines with or without seipin-NE trap were delipidated for 3 days, last 18 h with DGAT1 and DGAT2 inhibitors (DGATi), washed, treated with OA, fixed, stained, and imaged by wide-field microscopy. Deconvolved maximum intensity projections of z-stacks.

(D) Analysis of (C). Bars: mean ± SEM, n = 210–237 cells from 2 experiments. NE-associated LDs overlap with the NE by at least 1 pixel (72 nm). ***$p < 0.0005$ (unpaired t test).

(E) Stable seipin-NE-trapped cells were delipidated for 3 days, treated with OA for 1 h and processed for ET. Single 2-nm-thick tomogram slices and models of 3D reconstructions of NE-associated LDs (brown), NE (blue), and NE-LD contacts (red). Each row depicts an LD and its contact. Orange and blue arrowheads indicate NE-LD contacts and fiber-like connections between NE and LDs, respectively.

(F) Analysis of (E). Dimensions of NE-LD contacts from tomogram slices. n = 15 contacts from 14 LDs, 2 experiments.

(G) End-seipin-GFPx7 cells stably expressing LiveDrop-mCherry were delipidated for 2 days, treated with OA for 120 s, fixed, imaged by Airyscan microscopy, and processed for ET. Insets: three LiveDrop puncta with seipin association and corresponding tomograms of ER-LD contacts (orange arrowheads) and a 3D model of a reconstruction of an LD (brown), nearby ER (yellow), and its ER-LD contact (red). Same orientation of LDs in light microscopy images and tomograms. See also Figures S1 and S2.

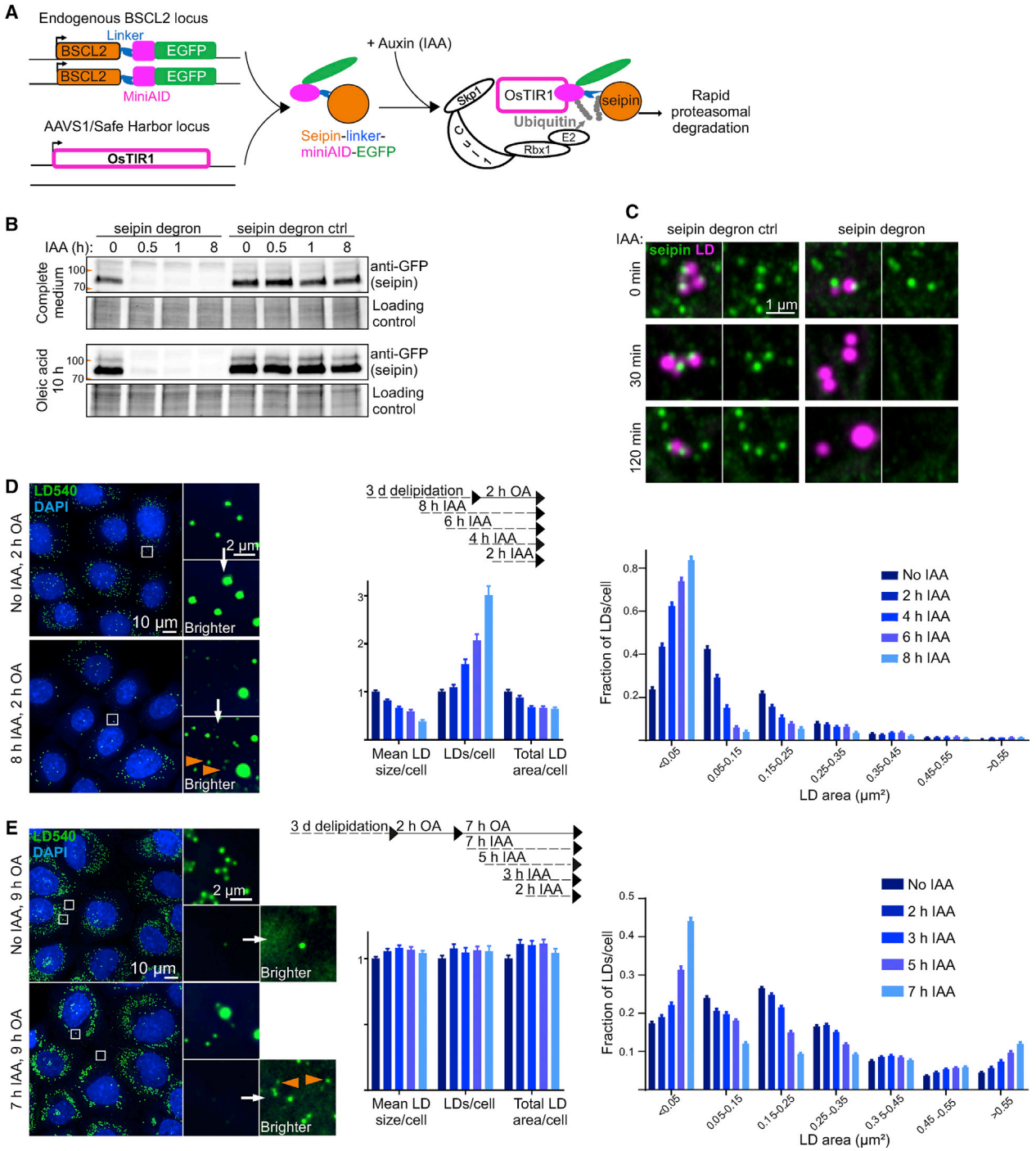

Figure 3. Effect of Acute Seipin Removal on LD Formation and Maintenance

(A) Schematic of auxin-inducible degron system.

(B) Immunoblots of seipin degron-A and seipin degron control (ctrl) cells treated with IAA.

(C) OA-loaded seipin degron ctrl and seipin degron-A cells were treated with IAA, fixed, and stained with LipidTOX Deep Red. Airyscan z-stack maximum intensity projections.

(D) Seipin degron-A cells were treated as indicated, fixed, stained, imaged by wide-field microscopy, and analyzed for LD sizes. Maximum intensity projections of deconvolved z-stacks. Orange arrowheads, tiny LDs in seipin-depleted cells. Bars: mean ± SEM, n = 197–237 cells, 2 experiments. IAA-treated cells are significantly different starting from 2 h IAA onward ($p < 0.005$, unpaired t test).

(E) Seipin degron-A cells were treated as indicated, imaged, and analyzed as in (D). Bars: mean ± SEM, n = 432–655 cells, 2 experiments. IAA-treated cells are significantly different starting from 3 h IAA onward ($p < 0.005$, unpaired t test).

See also Figures S2–S4.

Please cite this article in press as: Salo et al., Seipin Facilitates Triglyceride Flow to Lipid Droplet and Counteracts Droplet Ripening via Endoplasmic Reticulum Contact, Developmental Cell (2019), https://doi.org/10.1016/j.devcel.2019.05.016

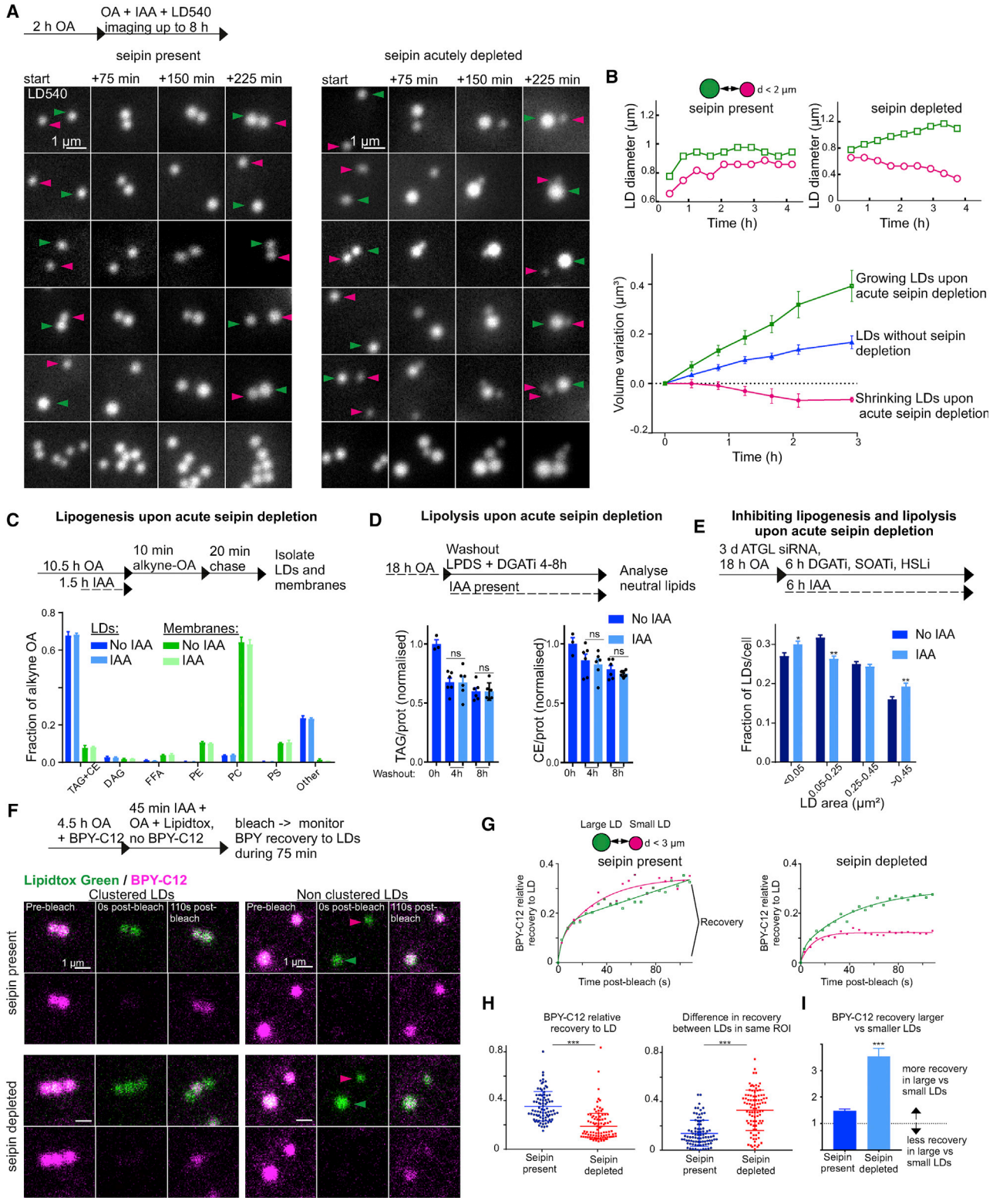

Figure 4. Seipin Removal from ER-LD Contacts Results in Inhomogeneous Neutral Lipid Partitioning to LDs

(A) Seipin degron ctrl and seipin degron-A cells were treated as indicated and imaged live with wide-field microscopy. LD pairs and clusters, first frames are 25–50 min after IAA addition for degron, 25–240 min for ctrl examples. Colored arrowheads indicate the same LDs in the first and last panels.

(B) Analysis of (A). Two nearby LDs were tracked over time and their sizes measured. Exemplary plots of nearby LD size changes and pooled data, n = 22–28 LDs, ± SEM, 2 experiments.

(legend continued on next page)

numerous tiny and some supersized LDs (Figure 3D). Overall, there was a net increase in the total number of LDs whose size was shifted toward tiny ones (Figure 3D), suggesting more nucleation events of LDs that failed to grow. Similar results were observed in both seipin degron lines but not with auxin treatment of ctrl cells (Figure S3A). Nevertheless, lipid analysis of nascent LDs isolated from control versus acutely seipin-depleted cells revealed no major alterations in phospholipid species, acyl chain length or saturation, or phospholipid/neutral lipid ratio (Figure S3B).

As the generation of numerous tiny LDs was the most prominent early feature of seipin-deficient cells on OA loading, we investigated if select proteins implicated in LD formation might be involved. We silenced ACSL3 (Kassan et al., 2013), Perilipin3/TIP47 (Bulankina et al., 2009), FIT2 (Choudhary et al., 2015), or Rab18 (Xu et al., 2018) in seipin degron cells and monitored the OA-induced appearance of LDs upon acute seipin removal. This revealed that knocking down Rab18 significantly attenuated the appearance of tiny LDs, while the other candidates tested had no obvious effect (Figure S3C). Similar results were obtained by Rab18 KO in this setting (Figures S3D and S3E). However, Rab18 KO alone without seipin removal did not dramatically alter LD size distribution (Figure S3F). Endogenously sfGFP-tagged Rab18 was present in a subset of LDs in control cells, in line with Martin et al. (2005) and Ozeki et al. (2005) and strikingly enriched in the tiny LDs of seipin-depleted cells (Figures S4A and S4B). Together, these results suggest that Rab18 facilitates the formation of tiny LDs in seipin-deficient cells. One possibility is that seipin prevents premature recruitment of Rab18 to LDs, thereby controlling LD nucleation. However, as Rab18 removal per se exhibited no major effects on LDs, the role of Rab18 in LD nucleation would only become apparent in seipin deficiency.

Seipin Is Required for LD Size Maintenance

We next performed experiments in seipin degron cells that were first OA loaded to induce LDs, followed by acute seipin removal in the continued presence of OA. These experiments revealed that seipin was required for LD maintenance: within a few hours of seipin removal, LDs became significantly more heterogeneous in size, with a shift toward larger and smaller LDs (Figure 3E). Similar results were observed in both seipin degron clones and also if OA loading was discontinued during seipin depletion, but not with auxin treatment of control cells (Figures S4C and S4D). These LD size changes appeared not to result from differential neutral lipid synthesis on LDs, as they were maintained when DGAT2 was inhibited (Figures S4E and S4F). Interestingly, the LD mean size, number, and total area were not markedly affected (Figures 3E, S4C, and S4D). Moreover, knocking out Rab18 did not inhibit the generation of small LDs in this setting (Figure S4G), suggesting that they are not formed *de novo*. Together, these data argue that nucleation of new tiny LDs did not explain the LD size heterogeneity developing upon seipin removal from existing LDs.

To further investigate the reasons underlying LD size heterogeneity upon acute seipin removal from pre-existing droplets, we performed live-cell imaging in the presence of OA and auxin. By tracking individual LDs for prolonged periods of time, we found that while LDs of control cells showed apparent steady growth rate, seipin-depleted LDs started to grow inhomogeneously in less than an hour after seipin depletion. Typically, in seipin-depleted cells, slightly larger LDs started to grow, while nearby smaller LDs stopped growing or appeared to shrink (Figures 4A and 4B). In these seipin-depleted cells, when we analyzed the growth dynamics of LDs close to a shrinking one, we found that the increase in size matches almost exactly the decrease in the size of the shrinking droplet, taking as a reference the normal growth of LDs containing seipin (Figure S5A). This observation points to the possibility that the smaller LD managed to transfer its content to the bigger one. The timescale and characteristics of LD size changes (minutes-hours of growing and shrinking) were not readily compatible with LD fusion, which is a rapid (<1 s) merging of two LDs (Thiam et al., 2013).

To assess if the observed LD size variation is due to altered fatty acid metabolism, we monitored OA metabolism between control and acutely seipin-depleted cells using click chemistry (Thiele et al., 2012). No differences in alkyne-oleate partitioning into various lipid species in isolated LDs or membrane fractions were observed (Figure 4C). This suggests that neutral lipid or phospholipid biosynthesis alterations were not responsible for the observed LD morphological phenotypes in seipin degron cells. Moreover, net lipolysis of neutral lipids was not affected upon acute seipin removal (Figure 4D), and inhibition of the lipases adipose triglyceride lipase (ATLG, by siRNA) and hormone-sensitive lipase (HSL, by inhibitor) did not prevent the inhomogeneous LD growth of seipin-depleted cells (Figure S5B). Finally, we concomitantly inhibited both *de novo* lipogenesis and lipolysis. Even under these conditions, seipin removal evoked a shift in LD sizes, albeit more modest, to larger and smaller ones (Figure 4E).

(C) Seipin degron-A cells were treated as indicated, LDs and membranes were isolated, followed by lipid extraction, click reaction, and thin-layer chromatography. Bars: mean fraction of alkyne-labeled lipid per group, ± SEM, n = 3, representative experiment repeated twice with similar results.

(D) Seipin degron-B cells were treated as indicated and lipid levels analyzed by high performance thin-layer chromatography. Bars: mean ± SEM, n = 3–6, 2 experiments.

(E) Seipin degron-A cells were incubated with adipose triglyceride lipase (ATGL) siRNAs for 3 days, including 18 h OA loading, and then kept in complete medium for 6 h ± IAA with DGAT1, DGAT2, and sterol O-acyltransferase inhibitors to inhibit *de novo* lipogenesis and hormone-sensitive lipase (HSL) inhibitor to inhibit lipolysis. LD size analysis as in Figure 3D. Bars: mean ± SEM, n = 394–364 cells, 2 experiments. *$p < 0.05$, **$p < 0.005$ (unpaired t test).

(F) Seipin degron ctrl and seipin degron-A cells were treated as indicated, LDs were photobleached and BPY recovery to LDs monitored by confocal imaging. Green and red arrowheads indicate larger and smaller LDs.

(G) Analysis of (F). Exemplary FRAP recovery curves of nearby large and small LDs from ctrl and seipin-depleted cells.

(H) Analysis of (F). Overall relative recovery (normalized pre- and postbleach) and difference in recovery between LDs in the same region of interest (ROI), n = 86–90 bleached LDs, 4 experiments. ***$p < 0.0005$ (Mann-Whitney test).

(I) Analysis of (F). Absolute BPY recovery in larger versus smaller nearby LDs, mean ± SEM, n = 32–35 LD pairs, 3 experiments. ***$p < 0.0005$ (unpaired t test). See also Figure S5.

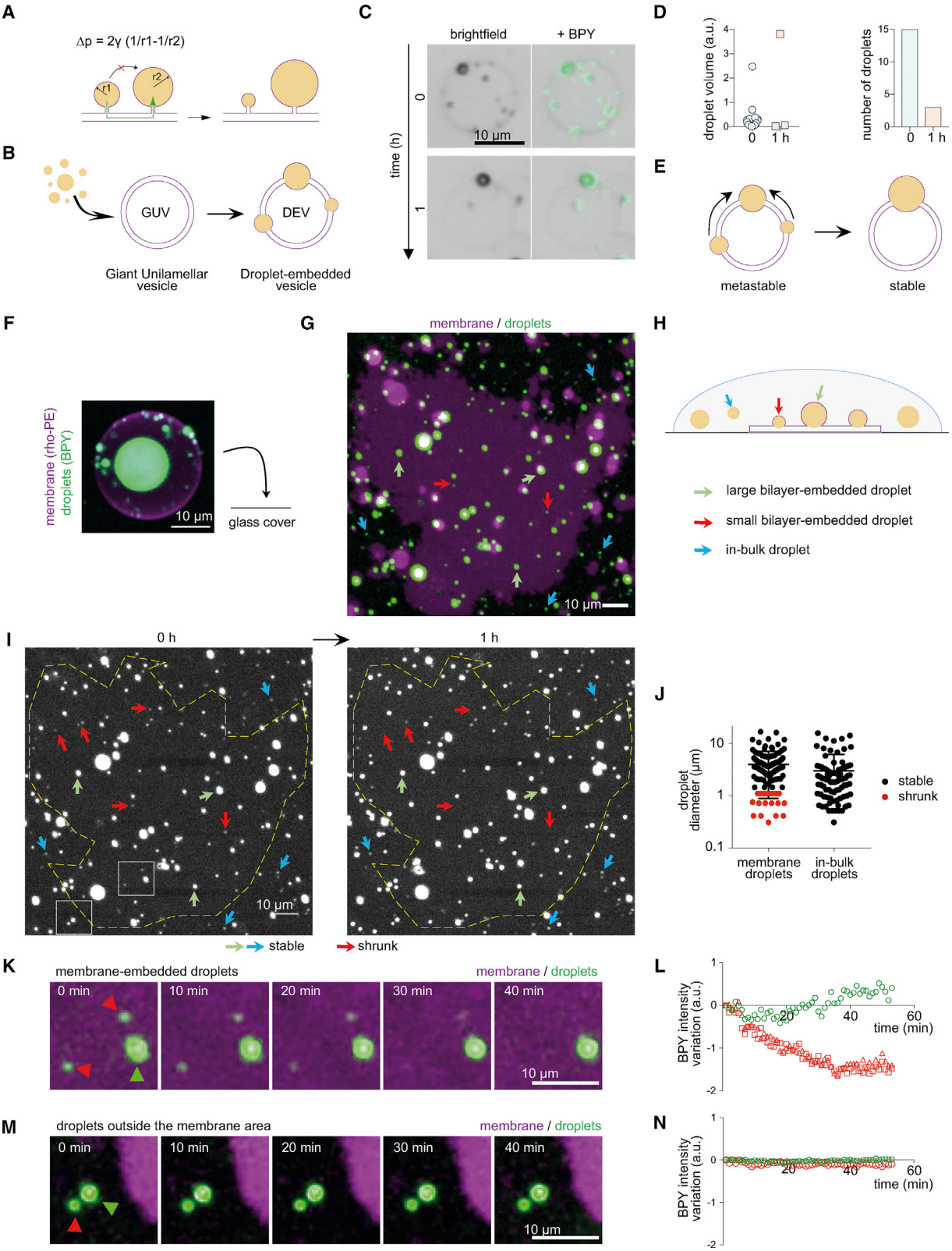

Figure 5. *In Vitro* Membrane-Embedded Droplets Destabilize by Ripening through the Bilayer

(A) Ripening principle: oil molecules transfer from smaller to bigger droplets through the bilayer due to pressure mismatch. Pressure, p, depends on the droplet monolayer surface tension, γ, and radius, r.

(legend continued on next page)

Since neither net lipid synthesis nor breakdown seemed to be clearly altered upon acute seipin depletion, we wondered if the transport of lipids between the ER and individual LDs is altered. To probe this, we incubated cells with Bodipy-C12 (BPY-C12) to label LDs, and studied fluorescence recovery after photobleaching (FRAP). Under these conditions, BPY fluorescence traces neutral lipid flux from the ER to LDs, as the majority of BPY signal was in neutral lipids in LDs isolated from both control and acutely seipin-depleted cells (Figure S5C). We found that in control cells, the recovery of neutral lipids to LDs was rapid and relatively homogenous (Figures 4F–4H and S5D). However, when seipin was acutely removed, this recovery was diminished and became strikingly inhomogeneous (Figures 4F–4H, S5D, and S5E). Further analysis revealed that larger LDs had the tendency to acquire more BPY signal than smaller LDs, and this was greatly accentuated upon acute seipin removal (Figures 4I and S5F). Moreover, neither the overall recovery nor the differential recovery between control and seipin-depleted cells required new triglyceride synthesis, as it was not altered by inhibiting both DGAT enzymes (Figure S5G). Finally, defective recovery of BPY-C12 to LDs was also observed in BSCL2 patient fibroblasts (Figure S5H). Overall, these data suggest that seipin controls the partitioning of neutral lipids between the ER and LD, and its absence inhibits the growth of smaller LDs.

Artificial LD Size Changes via Ripening

This phenotype of larger LDs growing in size at the expense of smaller ones is similar to what has been observed in adipocytes due to FSP27, also known as CIDE-C. This protein ensures transfer of neutral lipids from smaller to larger LDs via ripening at LD-LD contacts (Gong et al., 2011). However, the CIDE protein family members are not detectable at the mRNA level in A431 cells (www.proteinatlas.org), nor in proteomics of LDs isolated from A431 cells (Moessinger et al., 2011) (and data not shown). More importantly, the development of enlarging and shrinking LDs upon seipin removal did not necessitate direct LD-LD contacts. Therefore, we suspected that the observed process involved ripening, probably through the ER bilayer (Figure 5A). To test this hypothesis, we took advantage of the droplet-embedded vesicle (DEV) system (Chorlay and Thiam, 2018; Ben M'barek et al., 2017) to study communication between neutral lipid droplets. DEVs are giant unilamellar vesicles (GUVs) in which artificial LDs are incorporated between bilayer leaflets (Figure 5B). When multiple triolein droplets with various sizes were initially present in the DEV (Figure 5C), they disappeared to form one larger droplet within an hour (Figures 5C and 5D). This demonstrates that having many droplets in a bilayer is a metastable situation that will evolve to the more stable situation of one large droplet in the bilayer (Figure 5E).

The transition in droplet number and size (Figure 5D) occurred by rapid lateral fusion between droplets (Figures S6A and S6B). This was accentuated by the buoyancy of the droplets, which tended to regroup them at the apex of the DEV. As this limitation masked the possibility to detect ripening between droplets, which is a much slower process (Figure S6C) (Thiam and Forêt, 2016), we worked on flat membranes with droplets further apart from each other, labeling the membrane with rhodamine-phosphatidylethanolamine (PE) and the droplets with BPY. We made DEVs containing droplets in a wide size range and put them on a glass slide (Figure 5F), resulting in the spreading of the membrane. This generates droplets embedded in a flat bilayer and in-bulk droplets that are not membrane connected (Figures 5G and 5H). When following the droplets over time, we found that most small droplets connected to the bilayer shrank and eventually disappeared (Figures 5I, 5J, and S6D–S6F). In contrast, droplets of similar size, which were off the bilayer, remained intact (Figures 5I and 5J). We interpret this phenomenon as ripening, with smaller droplets leaking material to bigger ones. By quantifying BPY fluorescence intensity changes of nearby membrane-embedded droplets, we observed an increase in fluorescence in large droplets and a decrease in smaller droplets (Figures 5K, 5L, S6G, and S6H). In comparison, droplets of similar size difference but off the bilayer did not change in size or fluorescence intensity (Figures 5M, 5N, and S6I). These findings confirm a transfer of neutral lipids from smaller to bigger droplets and imply that this flux depends on membrane contact.

Together, these results suggest that in a protein-free situation, droplets in a bilayer are metastable and will ripen to yield one large droplet, by leakage of neutral lipids through the bilayer from smaller to larger droplets. The ripening mechanism is possible because of the solubility of the neutral lipids in the bilayer; droplets that are off the bilayer do not ripen regardless of their size because of the poorer solubility of neutral lipids in the aqueous phase.

(B) Principle of DEV formation.
(C) Time lapse of a DEV initially containing many droplets (t = 0 h) that become fewer and larger over time (t = 1 h).
(D) Quantification of the volume and number of the droplets in (C), between t = 0 h and t = 1 h.
(E) Many droplets in a bilayer form a metastable state that evolves into one droplet, reducing total surface.
(F) A DEV solution was placed on a coverslip onto which DEVs spread.
(G) The deposited DEV solution yielded flat membranes containing droplets, with non-embedded droplets around.
(H) Illustration of spread DEV with droplets in- and outside the membrane.
(I) Evolution of droplets of variable sizes, in- or outside bilayer. Smaller bilayer-embedded droplets (red arrows) shrunk over time, while bigger ones (green arrows) remained. Small droplets outside bilayer (blue arrows) did not shrink.
(J) Analysis of droplets in- and outside the bilayer, n ~ 90/group, 3 experiments.
(K) Upper inset in (I). In the bilayer, an example of small droplets nearby a larger one : small droplets slowly lost their content, based on BPY reporter,while the larger one acquired more BPY.
(L) quantification of BPY signal over time of the droplets shown in (K) (red triangle and square are for the smaller droplets and green circle is for the larger droplet).
(M) Lower inset in (I). Outside the bilayer, an example of a small droplet nearby a larger one : none of them change in size over time based on BPY signal.
(N) Quantification of BPY signal of the droplets shown in (M) (green for the larger droplet, red for the smaller droplet).
See also Figure S6.

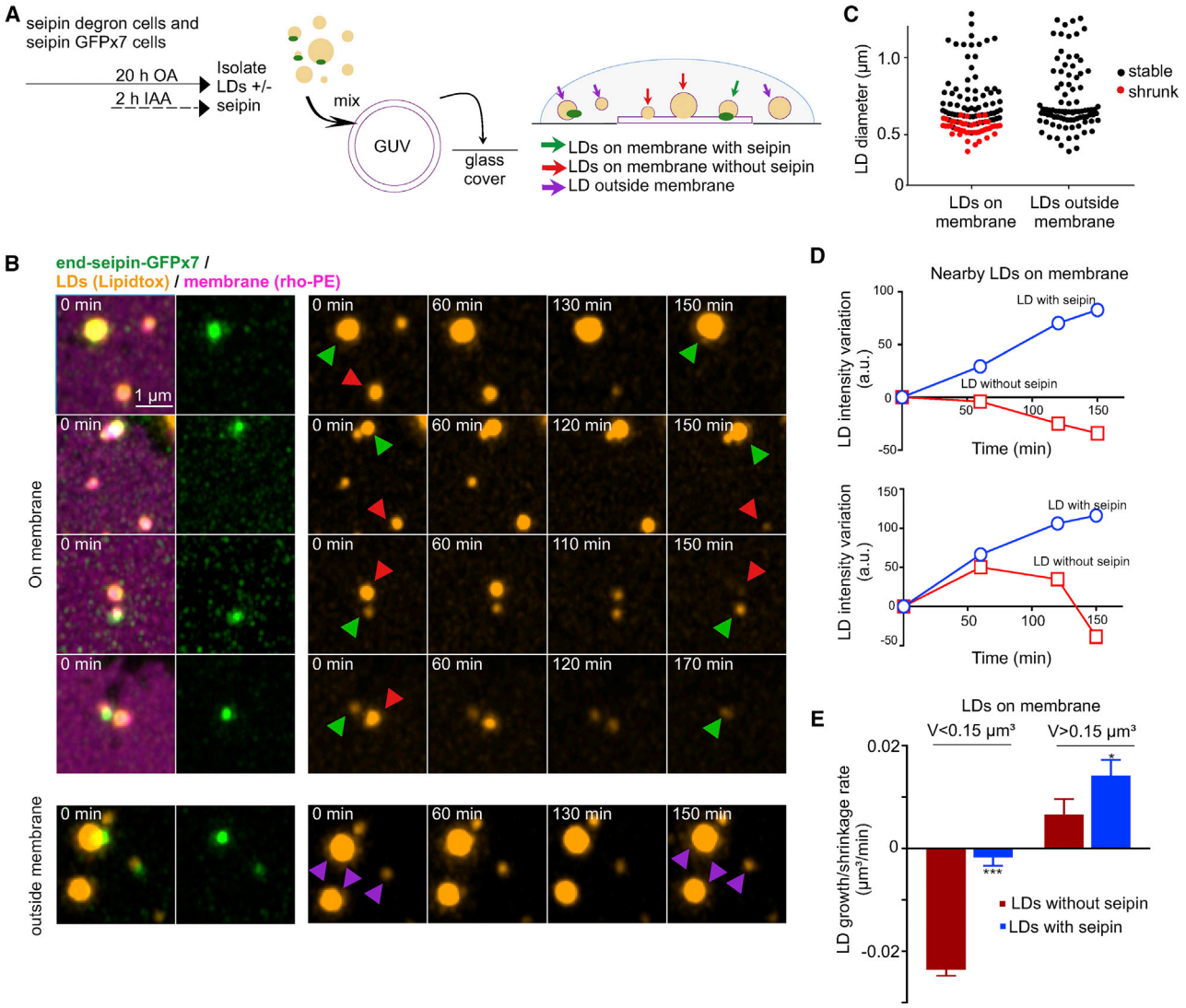

Figure 6. Seipin Counteracts Ripening *In Vitro*

(A) End-seipin-GFPx7 cells and seipin-degron-A cells were treated with OA and IAA as indicated, and LDs were isolated by gradient centrifugation. LD fractions were mixed with GUVs and placed on glass coverslips for time-lapse imaging, resulting in a system with membrane-embedded droplets with or without seipin.

(B) Examples of imaging as in (A), showing LDs of variable sizes ± seipin shrinking or growing over time. Note that droplets outside the membrane did not change in size.

(C) Analysis of droplets in- and outside the bilayer, n > 100 droplets, representative of 2 experiments.

(D) Examples of nearby LipidTox intensity changes over time from (A).

(E) Analysis of membrane-embedded droplet size changes from (A), mean ± SEM, n = 160–918 droplets from 12 flattened membrane systems, 2 experiments. ***p < 0.0005, *p < 0.05 Mann-Whitney test.

See also Figure S7.

Seipin Prevents Ripening *In Vitro*

We next performed *in vitro* experiments to investigate the effect of seipin on ripening-induced LD size changes. We isolated LDs ± fluorescently tagged seipin (from OA- and IAA-treated seipin degron and end-seipin-GFPx7 cells), mixed them with GUVs, and placed the mixture on glass for time-lapse imaging (Figures 6A and S7A). As for artificial LDs, also cellular LDs on the membrane experienced ripening, with smaller LDs shrinking and eventually disappearing, while larger LDs remained stable or grew (Figures 6B, 6C, and S7A). LDs that were outside the membrane did not change in size. When analyzing membrane-associated LDs over time, we found that seipin containing LDs shrunk less or grew more than similar sized LDs devoid of seipin (Figures 6B, 6D, 6E, S7B, and S7C). Overall, this suggests that seipin can facilitate LD growth and prevent ripening-induced shrinkage of small LDs *in vitro*.

Seipin Acts Locally to Facilitate Triglyceride Deposition in LDs

The *in vitro* experiments suggest that seipin acts droplet autonomously to promote LD growth. We utilized several approaches

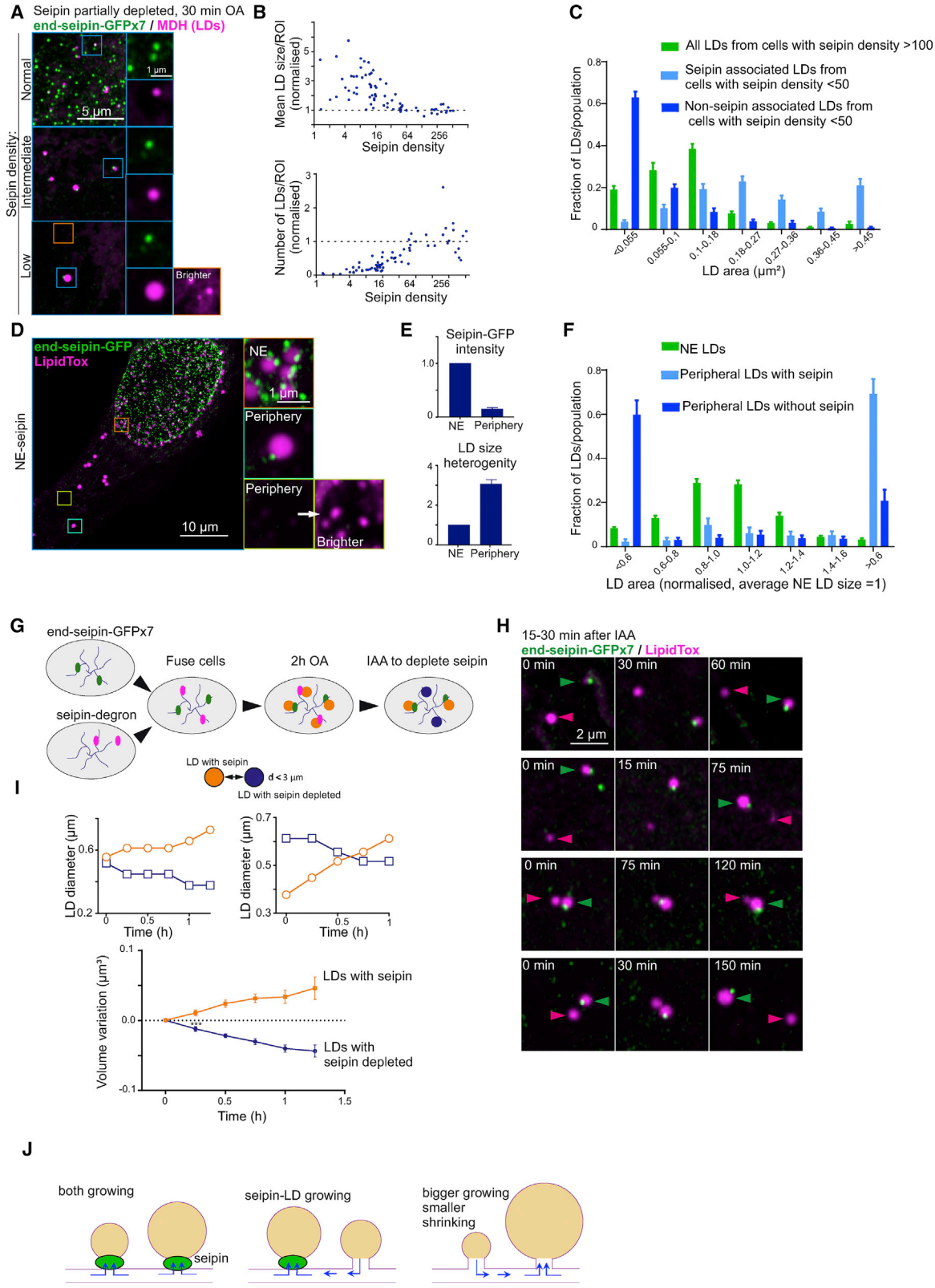

Figure 7. Seipin Functions Droplet Autonomously to Promote Triglyceride Delivery to LDs

(A) End-seipin-GFPx7 cells were treated with seipin siRNAs for 3 days in delipidation conditions, last 18 h with DGATi, followed by 5 min washout of DGATi and 30-min OA loading. Cells were fixed, LDs stained, and imaged by Airyscan microscopy. Maximum intensity projections of z stacks.

(legend continued on next page)

to investigate this further in the cellular context. First, we studied nascent LD growth in cells partially depleted of seipin by siRNAs or lentiviruses. We found that in cells with few remaining seipins, these seipins were invariably enriched at ER-LD contacts and the seipin-associated LDs grew more rapidly than LDs in cells with higher seipin content (Figures 7A–7C). This was noticeable already at 5 min of OA loading (Figure S7D) and striking by 30 min (Figures 7A–7C). In parallel, seipin-depleted cells accumulated tiny seipin-deficient LDs, typically at sites distant from seipin-associated LDs (Figures 7A and 7C). These results argue that seipin at the ER-LD neck facilitates LD growth.

We also employed the NE-trapped seipin cells to further scrutinize the spatial requirement of seipin in the ER network. We found that in those NE-trapped seipin cells where almost all seipins were trapped at the NE, the peripheral ER gave rise to tiny and supersized LDs, reminiscent of the seipin knockdown phenotype (Figures 7D and S7E). The tiny LDs in the cell periphery also displayed high motility (Figure S7F), similar to seipin-deficient cells (Salo et al., 2016). Remarkably, the few LDs in the cell periphery that still harbored seipin were supersized (Figures 7D–7F), providing additional evidence for a droplet growth promoting function of the protein.

Finally, we performed competition experiments employing heterologous cell fusions of delipidated seipin degron cells and end-seipin-GFPx7 cells, using conditions that also result in the fusion of ER membranes between cells (Salo et al., 2016). After fusion, we induced LDs by OA loading and subsequently depleted seipin from a subset of LDs. We then used live-cell imaging to track the fate of individual LDs that no longer harbored seipin and those nearby LDs that still contained seipin (Figures 7G and 7H). These experiments showed that seipin-containing LDs grew in size during the observation period, while nearby LDs, where seipin had been depleted, decreased in size (Figures 7H and 7I). Together, these findings provide evidence that seipin acts in a local, droplet-autonomous manner to facilitate triglyceride deposition in LDs and thereby enhance their growth.

DISCUSSION

Here, we developed a system to relocate endogenously GFP-tagged membrane protein(s) using a GFP nanobody tethered to a membrane of interest and applied it to trap seipin to the NE. This concentrated forming LDs at the NE, demonstrating that seipin can control the sites at which LDs start to develop. Moreover, this system enabled the first detailed analysis of the membrane architecture at ER-LD contact sites formed by seipin. We also developed a strategy to rapidly deplete endogenous seipins using the AID system. This is, to our knowledge, the first demonstration that AID works for human integral membrane proteins and was instrumental for revealing a role for seipin not only in forming but also in maintaining normal LDs.

By applying stringent delipidation followed by short OA loading, we generated relatively synchronously forming LDs that were distributed in a scattered manner throughout the ER, with seipins associated. Considering the dispersed localization of ACSL3, the key enzyme activating fatty acids for lipogenesis in A431 cells (Poppelreuther et al., 2018), it seems likely that neutral lipids are initially synthesized throughout the ER. Once their local concentration reaches a threshold, they phase separate and a LD is generated at a site marked by seipin. When observing the earliest LDs by EM, we found evidence that in A431 cells, LD budding has already taken place when the LD has reached a diameter of ~30 nm. The identification of such structures as presumptive LDs was based on correlation with seipin localization, typical electron dense interior, and bridging to the ER. Since the CLEM-based strategy involved partial seipin depletion, we cannot exclude the possibility that these LDs may somehow differ from LDs formed under normal seipin levels. Nevertheless, the nascent LDs grow by a coordinated flux of neutral lipid and expansion of the monolayer. Seipin localization at the LD contact is critical for this growth, based on the following observations: (1) LDs fail to grow normally in the absence of seipin; (2) if seipin is relocalized in the ER network, LD growth takes place at this relocated site; (3) if the number of seipins is reduced, LD growth is preferentially targeted at these sites; and (4) in a continuous ER network, LDs lacking seipin shrink, while those containing seipin grow (Figure 7J).

Our studies reveal a highly uniform neck with direct membrane continuity between the ER and LD monolayer at the site where seipin localizes. The neck has high membrane curvature, and seipin may be required to stabilize this site (Han et al., 2015). Recent structural insights into the human and *Drosophila* seipins with a 15- to 20-nm-wide ring-shaped structure intercalating into the bilayer (Sui et al., 2018; Yan et al., 2018) fit well with our measurement of the ER-LD membranous neck with a similar width and a plausible contact of the ER lumen with the LD monolayer. Moreover, if the budding droplets were restricted by the ring dimensions, they might indeed be in this size range. Interestingly, theoretical studies predicted a LD bud-off diameter of about 12 nm (Zanghellini et al., 2010).

(B) Analysis of (A). Seipin density: number of seipins/400 μm^2 ROI. LD data normalized to ROIs with seipin density >100. n = 73 ROIs, 2 experiments.
(C) Analysis of (A). Bars: mean ± SEM, n = 73 ROIs, 2 experiments.
(D) Seipin-NE-trapped cells were delipidated for 3 days, OA loaded for 2 h, fixed, stained, and imaged with Airyscan microscopy. Maximum intensity projection of a z-stack from a seipin NE-trapped cell.
(E) Analysis of (D). Bars: mean ± SEM, n = 12 cells. LD size heterogeneity is the SD of LD sizes/population.
(F) Analysis of (D). Bars: mean ± SEM, n = 12 cells.
(G) End-seipin-GFPx7 cells and seipin-degron-A cells expressing BFP-KDEL were delipidated for 2 days and co-plated for 1–2 days. Cells were fused with PEG and 1 h later treated with OA for 2 h. IAA was then added and fused cells were imaged live with Airyscan microscopy.
(H) Examples from live-cell imaging as in (G), showing nearby LDs where one LD has seipin depleted (magenta arrowheads) and one has seipin intact (green arrowheads).
(I) Analysis of (H). Two exemplary graphs of nearby LD size changes and pooled data, n = 14–15 LDs from 4 cells, 2 experiments. ***$p < 0.0005$ (unpaired t test).
(J) Schematic of the findings in this study.
See also Figure S7.

Considering ER and LDs as a joint system for neutral lipid partitioning has important implications for LD biology and understanding seipin function. In A431 cells, the ER membrane protein DGAT1 is the major enzyme responsible for triglyceride synthesis (Poppelreuther et al., 2018; Figure S4E), and therefore, continuous neutral lipid flux from the ER is critical for LD expansion. This flux toward the LD should lower the triglyceride content in the nearby ER and disfavor the formation of LDs adjacent to a forming droplet, which may explain why new droplets form at sites distant from pre-existing ones. Moreover, existing LDs would capture neutral lipids from the ER at the expense of forming LDs because of the lower internal pressure in bigger versus smaller LDs. Thus, neutral lipids would not avidly enter nascent LDs without a system that counteracts their high internal pressure and assists in the transfer of neutral lipids to them. We propose that seipin is a key component of such a system.

Our study indicates that seipin is continuously needed to maintain the normal LD size distribution. Seipin removal from pre-existing LDs provoked smaller LDs to gradually lose their contents at the expense of larger ones, evidently by lipid transfer via the ER bilayer as the process did not necessitate LD-LD contacts. This is analogous to our findings in seipin-deficient LDs connected to a model bilayer. Thus, acute seipin removal revealed a principle of LD ripening via the ER, where larger LDs acquire neutral lipid at the expense of smaller ones via the connecting lipid phase, and implies that seipin functions to counteract this phenomenon. Until now, the only example of ripening in the cell context is that of homotypic lipid exchange via LD-LD contacts regulated by FSP27 (Gong et al., 2011). The LD-stabilizing function of seipin is critical, as keeping LD diversity in number, lipid, and protein composition is key to metabolism (Thiam and Beller, 2017). Indeed, uncontrolled ripening may also contribute to impaired adipogenesis in BSCL2 knockout cells, where size heterogeneity of LDs preceded their eventual disappearance (Chen et al., 2012).

In conclusion, this study shows that seipin enables controlled LD growth by locally facilitating the partitioning of triglyceride from the ER to LDs and prevents their shrinkage by ripening. In principle, this could be achieved by facilitating transfer of neutral lipids from the ER to LDs or by preventing their leakage in the opposite direction. Since the effects of seipin depletion are most pronounced during active triglyceride synthesis and net transport toward LDs, we favor the former scenario. Seipin may directly transfer neutral lipids and/or modulate phospholipids at the ER-LD contact to enable LD growth. Indeed, the structural constraints at the ER-LD neck raise the possibility that seipin restricts the diameter of the LD neck and controls lipid diffusion. Considered together with previous data, the current observations begin to provide a glimpse into the fascinating mechanism by which LDs grow.

STAR★METHODS

Detailed methods are provided in the online version of this paper and include the following:

SUPPLEMENTAL INFORMATION

Supplemental Information can be found online at https://doi.org/10.1016/j.devcel.2019.05.016.

ACKNOWLEDGMENTS

We thank Mervi Lindman, Anna Uro and Katharina Ven for excellent technical assistance. We thank Biocenter Finland and HiLIFE Light and Electron microscopy, Functional genomics and Flow cytometry units. This study was supported by the Academy of Finland (grants 282192, 307415, and l312491 to E.I. and 1287975 to E.J.); LENDULET-BIOMAG grant (2018-342 to P.H. and A. Szkalisity); European Regional Development Funds (GINOP-2.3.2-15-2016-00006 to P.H. and A. Szkalisity), QLife program (to A.Santinho); Paris Sciences et Lettres installation grant (to A.R.T.); ANR-NanoDrop project (ANR-17-CE11-0003 to A.R.T.); and Mobil grant (ANR-18-CE11-0012-01 to A.R.T.). V.T.S. acknowledges support from the Finnish Medical, Paulo, Alfred Kordelin, Maud Kuistila, Biomedicum Helsinki, and Emil Aaltonen Foundation.

AUTHOR CONTRIBUTIONS

E.I., V.T.S., E.J., S.L., and A.R.T. designed the study. S.L. designed the cell lines and S.L. and V.T.S. generated the cell lines. V.T.S. performed and analyzed the cell experiments, with help from S.L. and M.H.-V. H.V. performed ET. V.T.S., H.V., and I.B. analyzed the EM data. A. Szkalisity and P.H. generated tools for image analysis. P.S. performed mass spectrometry. A. Santinho, A.R.T., H.Z., and V.T.S. performed and analyzed model membrane studies. C.T. and J.P. provided tools and techniques. E.I., V.T.S., and A.R.T. wrote the manuscript and all authors commented on the manuscript.

DECLARATION OF INTERESTS

The authors declare no competing interests.

Received: November 2, 2018
Revised: February 27, 2019
Accepted: May 3, 2019
Published: June 6, 2019

WEB RESOURCES

The Human Protein Atlas, www.proteinatlas.org

REFERENCES

Belevich, I., Joensuu, M., Kumar, D., Vihinen, H., and Jokitalo, E. (2016). Microscopy Image Browser: a platform for segmentation and analysis of multidimensional datasets. PLoS Biol. *14*, e1002340.

Ben M'barek, K., Ajjaji, D., Chorlay, A., Vanni, S., Forêt, L., and Thiam, A.R. (2017). ER membrane phospholipids and surface tension control cellular lipid droplet formation. Dev. Cell *41*, 591–604.e7.

Bi, J., Wang, W., Liu, Z., Huang, X., Jiang, Q., Liu, G., Wang, Y., and Huang, X. (2014). Seipin promotes adipose tissue fat storage through the ER Ca^{2+}-ATPase SERCA. Cell Metab. *19*, 861–871.

Binns, D., Lee, S., Hilton, C.L., Jiang, Q.X., and Goodman, J.M. (2010). Seipin is a discrete homooligomer. Biochemistry *49*, 10747–10755.

Bligh, E.G., and Dyer, W.J. (1959). A rapid method of total lipid extraction and purification. Can. J. Biochem. Physiol. *37*, 911–917.

Boutet, E., El Mourabit, H., Prot, M., Nemani, M., Khallouf, E., Colard, O., Maurice, M., Durand-Schneider, A.M., Chrétien, Y., Grès, S., et al. (2009). Seipin deficiency alters fatty acid Delta9 desaturation and lipid droplet formation in Berardinelli-Seip congenital lipodystrophy. Biochimie *91*, 796–803.

Bulankina, A.V., Deggerich, A., Wenzel, D., Mutenda, K., Wittmann, J.G., Rudolph, M.G., Burger, K.N.J., and Höning, S. (2009). TIP47 functions in the biogenesis of lipid droplets. J. Cell Biol. *185*, 641–655.

Cai, T., Shu, Q., Liu, P., Niu, L., Guo, X., Ding, X., Xue, P., Xie, Z., Wang, J., Zhu, N., et al. (2016). Characterization and relative quantification of phospholipids based on methylation and stable isotopic labeling. J. Lipid Res. *57*, 388–397.

Cai, Y., Goodman, J.M., Pyc, M., Mullen, R.T., Dyer, J.M., and Chapman, K.D. (2015). Arabidopsis seipin proteins modulate triacylglycerol accumulation and influence lipid droplet proliferation. Plant Cell *27*, 2616–2636.

Carpenter, A.E., Jones, T.R., Lamprecht, M.R., Clarke, C., Han Kan, I., Friman, O., Guertin, D.A., Han Chang, J., Lindquist, R.A., Moffat, J., et al. (2006). CellProfiler: image analysis software for identifying and quantifying cell phenotypes. Genome Biol. *7*, 100–110.

Cartwright, B.R., Binns, D.D., Hilton, C.L., Han, S., Gao, Q., and Goodman, J.M. (2015). Seipin performs dissectible functions in promoting lipid droplet biogenesis and regulating droplet morphology. Mol. Biol. Cell *26*, 726–739.

Chen, W., Chang, B., Saha, P., Hartig, S.M., Li, L., Reddy, V.T., Yang, Y., Yechoor, V., Mancini, M.A., and Chan, L. (2012). Berardinelli-seip congenital lipodystrophy 2/seipin is a cell-autonomous regulator of lipolysis essential for adipocyte differentiation. Mol. Cell. Biol. *32*, 1099–1111.

Chorlay, A., and Thiam, A.R. (2018). An asymmetry in monolayer tension regulates lipid droplet budding direction. Biophys. J. *114*, 631–640.

Choudhary, V., Ojha, N., Golden, A., and Prinz, W.A. (2015). A conserved family of proteins facilitates nascent lipid droplet budding from the ER. J. Cell Biol. *211*, 261–271.

Cui, X., Wang, Y., Tang, Y., Liu, Y., Zhao, L., Deng, J., Xu, G., Peng, X., Ju, S., Liu, G., et al. (2011). Seipin ablation in mice results in severe generalized lipodystrophy. Hum. Mol. Genet. *20*, 3022–3030.

de Chaumont, F., Dallongeville, S., Chenouard, N., Hervé, N., Pop, S., Provoost, T., Meas-Yedid, V., Pankajakshan, P., Lecomte, T., Le Montagner, Y., et al. (2012). Icy: an open BioImage informatics platform for extended reproducible research. Nat. Methods *9*, 690–696.

Elbashir, S.M., Harborth, J., Lendeckel, W., Yalcin, A., Weber, K., and Tuschl, T. (2001). Duplexes of 21 ± nucleotide RNAs mediate RNA interference in cultured mammalian cells. Nature *411*, 494–498.

Fei, W., Li, H., Shui, G., Kapterian, T.S., Bielby, C., Du, X., Brown, A.J., Li, P., Wenk, M.R., Liu, P., et al. (2011). Molecular characterization of seipin and its mutants: implications for seipin in triacylglycerol synthesis. J. Lipid Res. *52*, 2136–2147.

Fei, W., Shui, G., Gaeta, B., Du, X., Kuerschner, L., Li, P., Brown, A.J., Wenk, M.R., Parton, R.G., and Yang, H. (2008). Fld1p, a functional homologue of human seipin, regulates the size of lipid droplets in yeast. J. Cell Biol. *180*, 473–482.

Frangakis, A.S., and Hegerl, R. (2001). Noise reduction in electron tomographic reconstructions using nonlinear anisotropic diffusion. J. Struct. Biol. *135*, 239–250.

Friedman, J.R., Lackner, L.L., West, M., DiBenedetto, J.R., Nunnari, J., and Voeltz, G.K. (2011). ER tubules mark sites of mitochondrial division. Science *334*, 358–362.

Gangley, I.G., Kate, C., Bittova, L., and Pfeffer, S. (2005). Rab9 GTPase regulates late endosome size and requires effector interaction for its stability. Mol. Biol. Cell *15*, 5420–5430.

Goldstein, J.L., Basu, S.K., and Brown, M. (1983). Receptor-mediated endocytosis of low-density lipoprotein in cultured cells. Methods Enzymol. *98*, 241–260.

Gong, J., Sun, Z., Wu, L., Xu, W., Schieber, N., Xu, D., Shui, G., Yang, H., Parton, R.G., and Li, P. (2011). Fsp27 promotes lipid droplet growth by lipid exchange and transfer at lipid droplet contact sites. J. Cell Biol. *195*, 953–963.

Grippa, A., Buxó, L., Mora, G., Funaya, C., Idrissi, F.Z., Mancuso, F., Gomez, R., Muntanyà, J., Sabidó, E., and Carvalho, P. (2015). The seipin complex Fld1/Ldb16 stabilizes ER-lipid droplet contact sites. J. Cell Biol. *211*, 829–844.

Haimi, P., Uphoff, A., Hermansson, M., and Somerharju, P. (2006). Software tools for analysis of mass spectrometric lipidome data. Anal. Chem. *78*, 8324–8331.

Han, S., Binns, D.D., Chang, Y.F., and Goodman, J.M. (2015). Dissecting seipin function: the localized accumulation of phosphatidic acid at ER/LD junctions in the absence of seipin is suppressed by Sei1pΔNterm only in combination with Ldb16p. BMC Cell Biol. *16*, 29.

Hänninen, S., Batchu, K.C., Hokynar, K., and Somerharju, P. (2017). Simple and rapid biochemical method to synthesize labeled or unlabeled phosphatidylinositol species. J. Lipid Res. *58*, 1259–1264.

Hermansson, M., Uphoff, A., Käkelä, R., and Somerharju, P. (2005). Automated quantitative analysis of complex lipidomes by liquid chromatography/mass spectrometry. Anal. Chem. *77*, 2166–2175.

Herms, A., Bosch, M., Reddy, B.J.N., Schieber, N.L., Fajardo, A., Rupérez, C., Fernández-Vidal, A., Ferguson, C., Rentero, C., Tebar, F., et al. (2015). AMPK activation promotes lipid droplet dispersion on detyrosinated microtubules to increase mitochondrial fatty acid oxidation. Nat. Commun. *6*, 7176.

Hölttä-Vuori, M., Salo, V.T., Ohsaki, Y., Suster, M.L., and Ikonen, E. (2013). Alleviation of seipinopathy-related ER stress by triglyceride storage. Hum. Mol. Genet. *22*, 1157–1166.

Jacquier, N., Choudhary, V., Mari, M., Toulmay, A., Reggiori, F., and Schneiter, R. (2011). Lipid droplets are functionally connected to the endoplasmic reticulum in Saccharomyces cerevisiae. J. Cell Sci. *124*, 2424–2437.

Kamiyama, D., Sekine, S., Barsi-Rhyne, B., Hu, J., Chen, B., Gilbert, L.A., Ishikawa, H., Leonetti, M.D., Marshall, W.F., Weissman, J.S., et al. (2016). Versatile protein tagging in cells with split fluorescent protein. Nat. Commun. *7*, 11046.

Kassan, A., Herms, A., Fernández-Vidal, A., Bosch, M., Schieber, N.L., Reddy, B.J.N., Fajardo, A., Gelabert-Baldrich, M., Tebar, F., Enrich, C., et al. (2013). Acyl-CoA synthetase 3 promotes lipid droplet biogenesis in ER microdomains. J. Cell Biol. *203*, 985–1001.

Magré, J., Delépine, M., Khallouf, E., Gedde-Dahl, T., Van Maldergem, L., Sobel, E., Papp, J., Meier, M., Mégarbané, A., Bachy, A., et al. (2001). Identification of the gene altered in Berardinelli-Seip congenital lipodystrophy on chromosome 11q13. Nat. Genet. *28*, 365–370.

Martin, S., Driessen, K., Nixon, S.J., Zerial, M., and Parton, R.G. (2005). Regulated localization of Rab18 to lipid droplets: effects of lipolytic stimulation and inhibition of lipid droplet catabolism. J. Biol. Chem. *280*, 42325–42335.

Moessinger, C., Kuerschner, L., Spandl, J., Shevchenko, A., and Thiele, C. (2011). Human lysophosphatidylcholine acyltransferases 1 and 2 are located in lipid droplets where they catalyze the formation of phosphatidylcholine. J. Biol. Chem. *286*, 21330–21339.

Natsume, T., Kiyomitsu, T., Saga, Y., and Kanemaki, M.T. (2016). Rapid protein depletion in human cells by auxin-inducible degron tagging with short homology donors. Cell Rep. *15*, 210–218.

Niopek, D., Wehler, P., Roensch, J., Eils, R., and Di Ventura, B. (2016). Optogenetic control of nuclear protein export. Nat. Commun. *7*, 1–9.

Nishimura, K., Fukagawa, T., Takisawa, H., Kakimoto, T., and Kanemaki, M. (2009). An auxin-based degron system for the rapid depletion of proteins in nonplant cells. Nat. Methods *6*, 917–922.

Ohsaki, Y., Sołtysik, K., and Fujimoto, T. (2017). The lipid droplet and the endoplasmic reticulum. Adv. Exp. Med. Biol. *997*, 111–120.

Ozeki, S., Cheng, J., Tauchi-Sato, K., Hatano, N., Taniguchi, H., and Fujimoto, T. (2005). Rab18 localizes to lipid droplets and induces their close apposition to the endoplasmic reticulum-derived membrane. J. Cell Sci. *118*, 2601–2611.

Pagac, M., Cooper, D.E., Qi, Y., Lukmantara, I.E., Mak, H.Y., Wu, Z., Tian, Y., Liu, Z., Lei, M., Du, X., et al. (2016). Seipin regulates lipid droplet expansion and adipocyte development by modulating the activity of glycerol-3-phosphate acyltransferase. Cell Rep. *17*, 1546–1559.

Penno, A., Hackenbroich, G., and Thiele, C. (2013). Phospholipids and lipid droplets. Biochim. Biophys. Acta *1831*, 589–594.

Pfisterer, S.G., Gateva, G., Horvath, P., Pirhonen, J., Salo, V.T., Karhinen, L., Varjosalo, M., Ryhänen, S.J., Lappalainen, P., and Ikonen, E. (2017). Role for formin-like 1-dependent acto-myosin assembly in lipid droplet dynamics and lipid storage. Nat. Commun. *8*, 14858.

Pol, A., Gross, S.P., and Parton, R.G. (2014). Review: Biogenesis of the multifunctional lipid droplet: lipids, proteins, and sites. J. Cell Biol. *204*, 635–646.

Poppelreuther, M., Sander, S., Minden, F., Dietz, M.S., Exner, T., Du, C., Zhang, I., Ehehalt, F., Knüppel, L., Domschke, S., et al. (2018). The metabolic capacity of lipid droplet localized acyl-CoA synthetase 3 is not sufficient to support local triglyceride synthesis independent of the endoplasmic reticulum in A431 cells. Biochim. Biophys. Acta Mol. Cell Biol. Lipids *1863*, 614–624.

Rambold, A.S., Cohen, S., and Lippincott-Schwartz, J. (2015). Fatty acid trafficking in starved cells: regulation by lipid droplet lipolysis, autophagy, and mitochondrial fusion dynamics. Dev. Cell *32*, 678–692.

Ran, F.A., Hsu, P.D., Wright, J., Agarwala, V., Scott, D.A., and Zhang, F. (2013). Genome engineering using the CRISPR-Cas9 system. Nat. Protoc. *8*, 2281–2308.

Rothbauer, U., Zolghadr, K., Tillib, S., Nowak, D., Schermelleh, L., Gahl, A., Backmann, N., Conrath, K., Muyldermans, S., Cardoso, M.C., et al. (2006). Targeting and tracing antigens in live cells with fluorescent nanobodies. Nat. Methods *3*, 887–889.

Salo, V.T., Belevich, I., Li, S., Karhinen, L., Vihinen, H., Vigouroux, C., Magré, J., Thiele, C., Hölttä-Vuori, M., Jokitalo, E., et al. (2016). Seipin regulates ER–lipid droplet contacts and cargo delivery. EMBO J. *24*, 2699–2716.

Salo, V.T., and Ikonen, E. (2019). Moving out but keeping in touch: contacts between endoplasmic reticulum and lipid droplets. Curr. Opin. Cell Biol. *57*, 64–70.

Schindelin, J., Arganda-Carreras, I., Frise, E., Kaynig, V., Longair, M., Pietzsch, T., Preibisch, S., Rueden, C., Saalfeld, S., Schmid, B., et al. (2012). Fiji: an open-source platform for biological-image analysis. Nat. Methods *9*, 676–682.

Schuldiner, M., and Bohnert, M. (2017). A different kind of love – lipid droplet contact sites. Biochim. Biophys. Acta Mol. Cell Biol. Lipids *1862*, 1188–1196.

Seemann, J., Jokitalo, E.J., and Warren, G. (2000). The role of the tethering proteins p115 and GM130 in transport through the Golgi apparatus in vivo. Mol. Biol. Cell *11*, 635–645.

Sommer, C., Straehle, C., Ullrich, K., and Hamprecht, F.A. (2011). ILASTIK: interactive learning and segmentation toolkit. In Eighth IEEE International Symposium on Biomedical Imaging (ISBI): From NANO to Macro, pp. 230–233.

Sosa, B.A., Rothballer, A., Kutay, U., and Schwartz, T.U. (2012). LINC complexes form by binding of three KASH peptides to domain interfaces of trimeric SUN proteins. Cell *149*, 1035–1047.

Spandl, J., White, D.J., Peychl, J., and Thiele, C. (2009). Live cell multicolor imaging of lipid droplets with a new dye, LD540. Traffic *10*, 1579–1584.

Stanley, S.A., Kelly, L., Latcha, K.N., Schmidt, S.F., Yu, X., Nectow, A.R., Sauer, J., Dyke, J.P., Dordick, J.S., and Friedman, J.M. (2016). Bidirectional electromagnetic control of the hypothalamus regulates feeding and metabolism. Nature *531*, 647–650.

Sui, X., Arlt, H., Brock, K.P., Lai, Z.W., DiMaio, F., Marks, D.S., Liao, M., Farese, R.V., and Walther, T.C. (2018). Cryo-electron microscopy structure of the lipid droplet-formation protein seipin. J. Cell Biol. *217*, 4080–4091.

Sun, X., Zhang, A., Baker, B., Sun, L., Howard, A., Buswell, J., Maurel, D., Masharina, A., Johnsson, K., Noren, C.J., et al. (2011). Development of SNAP-tag fluorogenic probes for wash-free fluorescence imaging. Chembiochem *12*, 2217–2226.

Szymanski, K.M., Binns, D., Bartz, R., Grishin, N.V., Li, W.P., Agarwal, A.K., Garg, A., Anderson, R.G.W., and Goodman, J.M. (2007). The lipodystrophy protein seipin is found at endoplasmic reticulum lipid droplet junctions and is important for droplet morphology. Proc. Natl. Acad. Sci. USA *104*, 20890–20895.

Talukder, M.M.U., Sim, M.F.M., O'Rahilly, S., Edwardson, J.M., and Rochford, J.J. (2015). Seipin oligomers can interact directly with AGPAT2 and lipin 1, physically scaffolding critical regulators of adipogenesis. Mol. Metab. *4*, 199–209.

Thiam, A.R., and Beller, M. (2017). The why, when and how of lipid droplet diversity. J. Cell Sci. *130*, 315–324.

Thiam, A.R., Farese, R.V., and Walther, T.C. (2013). The biophysics and cell biology of lipid droplets. Nat. Rev. Mol. Cell Biol. *14*, 775–786.

Thiam, A.R., and Forêt, L. (2016). The physics of lipid droplet nucleation, growth and budding. Biochim. Biophys. Acta *1861*, 715–722.

Thiele, C., Papan, C., Hoelper, D., Kusserow, K., Gaebler, A., Schoene, M., Piotrowitz, K., Lohmann, D., Spandl, J., Stevanovic, A., et al. (2012). Tracing fatty acid metabolism by click chemistry. ACS Chem. Biol. *7*, 2004–2011.

Tian, Y., Bi, J., Shui, G., Liu, Z., Xiang, Y., Liu, Y., Wenk, M.R., Yang, H., and Huang, X. (2011). Tissue-autonomous function of Drosophila seipin in preventing ectopic lipid droplet formation. PLoS Genet. *7*, e1001364.

Walther, T.C., Chung, J., and Farese, R.V., Jr. (2017). Lipid droplet biogenesis. Annu. Rev. Cell Dev. Biol. *33*, 491–510.

Wang, H., Becuwe, M., Housden, B.E., Chitraju, C., Porras, A.J., Graham, M.M., Liu, X.N., Thiam, A.R., Savage, D.B., Agarwal, A.K., et al. (2016). Seipin is required for converting nascent to mature lipid droplets. Elife *5*, 133–150.

Weinberger, A., Tsai, F.C., Koenderink, G.H., Schmidt, T.F., Itri, R., Meier, W., Schmatko, T., Schröder, A., and Marques, C. (2013). Gel-assisted formation of giant unilamellar vesicles. Biophys. J. *105*, 154–164.

Welte, M.A. (2015). Expanding roles for lipid droplets. Curr. Biol. *25*, R470–R481.

Wilfling, F., Wang, H., Haas, J.T., Krahmer, N., Gould, T.J., Uchida, A., Cheng, J.X., Graham, M., Christiano, R., Fröhlich, F., et al. (2013). Triacylglycerol synthesis enzymes mediate lipid droplet growth by relocalizing from the ER to lipid droplets. Dev. Cell *24*, 384–399.

Wolinski, H., Hofbauer, H.F., Hellauer, K., Cristobal-Sarramian, A., Kolb, D., Radulovic, M., Knittelfelder, O.L., Rechberger, G.N., and Kohlwein, S.D. (2015). Seipin is involved in the regulation of phosphatidic acid metabolism at a subdomain of the nuclear envelope in yeast. Biochim. Biophys. Acta *1851*, 1450–1464.

Xu, D., Li, Y., Wu, L., Li, Y., Zhao, D., Yu, J., Huang, T., Ferguson, C., Parton, R.G., Yang, H., et al. (2018). Rab18 promotes lipid droplet (LD) growth by tethering the ER to LDs through SNARE and NRZ interactions. J. Cell Biol. *217*, 975–995.

Yan, R., Qian, H., Lukmantara, I., Gao, M., Du, X., Yan, N., and Yang, H. (2018). Human seipin binds anionic phospholipids. Dev. Cell *47*, 248–256.e4.

Zanghellini, J., Wodlei, F., and von Grünberg, H.H. (2010). Phospholipid demixing and the birth of a lipid droplet. J. Theor. Biol. *264*, 952–961.

STAR★METHODS

KEY RESOURCES TABLE

REAGENT or RESOURCE	SOURCE	IDENTIFIER
Antibodies		
rabbit polyclonal anti-GFP (IB: 1:10 000)	Abcam	Cat# ab290; RRID: AB_303395
rabbit polyclonal anti-Rab18 (IB 1:800)	Sigma-Aldrich	Cat# SAB4200173; RRID:AB_10638775
mouse polyclonal anti-ACSL3 (IF 1:200)	Abnova	Cat# H00002181-B01P; RRID:AB_10549799
rabbit polyclonal anti-TIP47 (IF: 1:100)	Proteintech	Cat# 10694–1-AP, RRID:AB_2297252
rabbit polyclonal anti-seipin (IB: 1:500)	This study	N/A
Bacterial and Virus Strains		
MISSION shBSCL2 lentivirus	Sigma-Aldrich	Cat# TRCN0000118734
BL21(DE3) cells	Merck	Cat# 69450-3
Chemicals, Peptides, and Recombinant Proteins		
Monodansylpentane/AUTOdot (100 μM)	Abgent	Cat# SM1000a
HCS LipidTox Deep Red (1:500-1:2000)	Thermo Fisher Scientific	Cat# H34477
HCS LipidTox Green (1:1000)	Thermo Fisher Scientific	Cat# H34475
LD540 (fixed cells 0.1 μg/ml, live cells 0.05 μg/ml)	Princeton BioMolecular Research (Spandl et al., 2009)	N/A
DAPI (10μg/ml)	Sigma-Aldrich	Cat# D9542
Prolong Live Anti-Fade (1:100)	Thermo Fisher Scientific	Cat# P36975
Lipofectamine LTX and Plus Reagent	Thermo Fisher Scientific	Cat# 15338100
PEG 1500	Sigma-Aldrich	Cat# 10783641001 Roche
DGAT1 inhibitor (5 μM)	Sigma-Aldrich	Cat# PZ0207
DGAT2 inhibitor (5 μM)	Sigma-Aldrich	Cat# PZ0233
SOAT inhibitor (2 μg/ml)	Sigma-Aldrich	Cat# S9318
HSL inhibitor (5 μM)	Cayman Chemical	Cat# CAY10499
Indole-3-acetic acid sodium, IAA (500 μM);	Santa Cruz	Cat# sc-215171
BODIPY 558/568 C12 (1 μM)	Thermo Fisher Scientific	Cat# D3835
Bodipy 493/503 (0.1 mg/ml)	Thermo Fisher Scientific	Cat# D3922
Cell-SIR647 (0.3 μM)	New England BioLabs	Cat# S9102S
CellTracker Red (1:500)	Thermo Fisher Scientific	Cat# C34552
Human fibronectin	Sigma-Aldrich	Cat# 11051407001 Roche
Puromycin (1 μg/ml)	Sigma-Aldrich	Cat# P8833
Geneticin, G418 (0.6 mg/ml)	Thermo Fisher	Cat# 11811-031 Gibco
Blasticidin (5 μg/ml)	Thermo Fisher	Cat# A1113904 Gibco
Zeocin (0.2 mg/ml)	Thermo Fisher	Cat# R25001 Gibco
Glyceryl trioleate (triolein)	Sigma-Aldrich	Cat# T7140
Phospholipids for model membrane studies	Avanti Polar Lipids	https://avantilipids.com/
Phospholipid standards for mass spectrometry	Prepared as described (Hänninen et al., 2017; Hermansson et al., 2005)	N/A
Bovine Serum Albumin	Sigma-Aldrich	Cat# A7906-100G
Sucrose 99,5%	Sigma-Aldrich	Cat# S59378
Polybrene (6 μg/ml)	Sigma-Aldrich	Cat# H9268
Alkyne-oleate, Alkyne lipid standards, 3-azido-7-hydroxycoumarin for click reactions	Prepared as described (Thiele et al., 2012)	N/A
LPDS (lipoprotein-deficient serum)	Prepared as described (Goldstein et al., 1983)	N/A

(*Continued on next page*)

Continued

REAGENT or RESOURCE	SOURCE	IDENTIFIER
Fluorobrite DMEM	Thermo Fisher	Cat# A1896702
Paraformaldehyde for light microscopy	Sigma-Aldrich	Cat# P-6148
Paraformaldehyde for EM and CLEM	Electron Microscopy Sciences	Cat# EMS-15710
Oleic acid	Sigma-Aldrich	Cat# O-1383
Critical Commercial Assays		
DC protein assay	Bio-Rad	Cat# 5000112
Experimental Models: Cell Lines		
A431 cells	ATCC	Cat# CRL-1555
Primary human fibroblasts	Coriell Cell Repositories	Cat# GMO1650; Cat# GM00323
BSCL2 patient fibroblasts	Boutet et al., 2009; Salo et al., 2016	N/A
Oligonucleotides		
GL2/Ctrl siRNA, sense: CGUACGCGGAAUACUUCGA	Sigma (Elbashir et al., 2001)	N/A
Seipin siRNA, Stealth, target cDNA: GACACCGCTTC TCTTTGCAGGTTAA	Invitrogen (Hölttä-Vuori et al., 2013)	N/A
TIP47/PLIN3 siRNA, sense: CAGAGCUACUUCGU ACGUC	Ambion (Gangley et al., 2005)	N/A
SUN2 siRNA 1 Silencer select, sense: CAACAGCA CUAUCUCCAGUtt	Ambion, Thermo Fisher	s24465 Cat# 4392420
SUN2 siRNA 2 Silencer select, sense: GGAAAUCC AGCAACAUGAAtt	Ambion, Thermo Fisher	s24466, Cat# 4427037
SUN 1 siRNA 1 Silencer select, sense: CAAUCAGUGCGGUUGGUGAtt	Ambion, Thermo Fisher	s23630, Cat# 4392420
Rab18 siRNA, target cDNA: CCAGGCCAATTTATA ACTAAA	Qiagen	N/A
FITM2 siRNA, sense: GGACAUACGGGUUUUGGUAtt	Ambion, Thermo Fisher	s43312 Cat# 4392420
ACSL3 siRNA, sense: GGAACUAACUGAACUAGCU	Ambion, Thermo Fisher (Salo et al., 2016)	s4997; Cat# 4390824
ATGL siRNA, Silencer select, sense: CUUUACUCC UGAGAACUUUtt	Ambion, Thermo Fisher	s32683, Cat# 4392420
sgRNA Seipin endogenous tagging sense: caccgTGCTCTAGTTCCTGAAGAAA	Salo et al., 2016	N/A
sgRNA AAVS1 Safe Harbor integration sense: caccGTCACCAATCCTGTCCCTAG	This study	N/A
Human BSCL2 genomic PCR sense: CAGGCTCCTGGGAAGATGCA	This study	N/A
Human BSCL2 genomic PCR antisense: CATGGGGGACACAGGGTGTTC	This study	N/A
sgRNA ASCL3 endogenous tagging sense: caccgAGAAAATAATTATTCTCTTC	This study	N/A
sgRNA RAB18 endogenous tagging sense: caccGAACGGGGTCAGGATGGACG	This study	N/A
sgRNA RAB18 knockout: caccgTCCTCATCATCGGCGAGAGT	This study	N/A
Human BSCL2 shRNA target sequence: CCGCTTCTCTTTGCAGGTTAA	Sigma	Cat# TRCN0000118734
Recombinant DNA		
pSNAPf-C1	Michael Davidson, Florida State University	Addgene #58186
pHRm-NLS-dCas9-GFP11x7-NLS-P2A-BFP-NLS	Kamiyama et al., 2016	Addgene #70224
pSpCas9(BB)-2A-GFP (PX458)	Ran et al., 2013	Addgene #48138

(*Continued on next page*)

Continued

REAGENT or RESOURCE	SOURCE	IDENTIFIER
pGL3-sgRNA(BbsI)-Cas9-T2A-mCherry-P2A-Puro	Salo et al., 2016	N/A
pGL3-basic-BSCL2-sfGFP(C) HDR template	Salo et al., 2016	N/A
pSH-EFIRES-P-GFP(1-10)opti AAVS1 Safe Harbor integration plasmid	This study	N/A
sfGFP-ER-3	Michael Davidson, Florida State University	Addgene #56482
pGL3-Basic-ACSL3-sfGFP(C) HDR template	This study	N/A
pGL3-Basic-Rab18-sfGFP(N) HDR template	This study	N/A
pVQ CMV NanoV1-2a-EGFP ferritin	Stanley et al., 2016	Addgene #79649
pEFIRES-P-NanoV1-3xFlag-GS3-KASH2	This study	N/A
pcDNA3.1(+)-Sun2	This study	N/A
pSH-PGK-NanoV1-3xFlag-GS3-KASH2-EFIRES-P-BFP-KDEL AAVS1/Safe Harbor integration plasmid	This study	N/A
pSH-CMVTOIRES-BSD-SUN2 AAVS1/Safe Harbor integration plasmid	This study	N/A
pMK287 (mAID-Hygro)	Natsume et al., 2016	Addgene #72825
pGL3-basic-BSCL2-miniAID-mEGFP(C) HDR template	This study	N/A
pMK243 (Tet-OsTIR1-PURO)	Natsume et al., 2016	Addgene #72835
pSH-EFIRES-P-OsTIR1-NES21 AAVS1/Safe Harbor integration plasmid	This study	N/A
pSH-EFIRES-P-NES2-OsTIR1 AAVS1/Safe Harbor integration plasmid	This study	N/A
BFP-KDEL	Friedman et al., 2011	Addgene #49150
LiveDrop-mCherry	Wang et al., 2016	N/A
pGEX-2T expression vector	GE Healthcare	Cat# GE28-9546-53
Software and Algorithms		
ImageJ FIJI	Schindelin et al., 2012	https://fiji.sc/
CellProfiler	Carpenter et al., 2006	https://cellprofiler.org/
Matlab	MathWorks	https://www.mathworks.com/products/matlab.html
ICY	de Chaumont et al., 2012	http://icy.bioimageanalysis.org/
Ilastik	Sommer et al., 2011	https://www.ilastik.org/
Huygens Professional	Scientific Volume Imaging	https://svi.nl/Huygens-Professional
Graphpad Prism	GraphPad Software	https://www.graphpad.com/scientific-software/prism/
MIB	Belevich et al., 2016	http://mib.helsinki.fi/
Amira	Thermo Fisher	N/A
QuanLynx	Waters	http://www.waters.com
LIMSA	Haimi et al., 2006	http://www.helsinki.fi/science/lipids/software.html
CorelDraw	Corel Corporation	https://www.corel.com/en/
Microsoft Excel	Microsoft	https://www.microsoft.com
Corel PHOTO-PAINT	Corel Corporation	https://www.corel.com/en/
Other		
8-well Lab-Tek II #1.5 coverglass slides	Thermo Fisher	Cat# 155409
#1.5 polymer μ-slide 8 well ibiTreat chambers	ibidi	Cat# 80826
High performance thickness no. $1^{1/2}$ cover glasses	Zeiss	Cat# 474030-9000-000
Gene Frame double sided tape	Thermo Fisher	Cat# AB-0576
ECL Clarity	Bio-Rad	Cat# 170-5060

(*Continued on next page*)

Continued

REAGENT or RESOURCE	SOURCE	IDENTIFIER
ECL Clarity Max substrate	Bio-Rad	Cat# 170-5062
Affi-10-Gel	Bio-Rad	Cat# 153-6046
Glutathionine sepharose	GE Healthcare	Cat# 17-0756-01

CONTACT FOR REAGENT AND RESOURCE SHARING

Further information and requests for resources and reagents should be directed to and will be fulfilled by the Lead Contact, Elina Ikonen (elina.ikonen@helsinki.fi). Requests will be handled according to the University of Helsinki policies regarding MTA and related matters.

EXPERIMENTAL MODEL AND SUBJECT DETAILS

Cell Culture and Cell Treatments

Cell Culture

A431 cells (ATCC CRL-1555, sex: female) were maintained in Dulbecco's modified Eagle's medium containing 10% fetal bovine serum (FBS), penicillin/streptomycin (100 U/ml each), L-glutamine (2 mM) at 37°C in 5% CO_2. Human primary fibroblasts were cultured in MEM, with 15% non-heat-inactivated FBS supplemented with penicillin/streptomycin (100 U/ml each) and L-glutamine (2 mM) at 37°C in 5% CO_2. Control human primary fibroblasts were from Coriell Cell Repositories (GM01650, sex: female; and GM00323, sex: male, designated as controls 1 and 2 in this study). BSCL2 patient fibroblasts S3, sex: male and S5, sex: male, were established from forearm skin biopsies of patients described in (Boutet et al., 2009) and have been previously characterized in (Salo et al., 2016). All cell lines were regularly tested negative for mycoplasma contamination using PCR.

Transfection, Delipidation, DGATi Treatments, LD Induction, Seipin Depletion with IAA and SNAP-Labeling

Transfections of plasmids (Lipofectamine LTX with PLUS Reagent) and siRNAs (HiPerfect) were carried out according to the manufacturer's instructions. Cells were delipidated by culturing in serum-free medium supplemented with 5% LPDS for indicated times. Where indicated, for more stringent delipidation cells were additionally incubated with DGAT1 and DGAT2 inhibitor for the final 18 h. DGATi indicates treatment with both DGAT1 and DGAT2 inhibitors. For LD induction cells were supplemented with 0.2 mM OA (final concentration, OA in complex with BSA in 8:1 molar ratio prepared in serum-free DMEM or FluoroBrite DMEM as described (Hölttä-Vuori et al., 2013)) for indicated times. For depletion of seipin, IAA was added to the medium for indicated times, vehicle control was Milli-Q-H_2O (1:100). SNAP-labeling was done for 5 min at +37°C, Cell-SIR647 was applied in 5% LPDS containing medium followed by 3 washes with phosphate buffered saline (PBS). SNAP-labeling was performed 2-4 h prior to imaging experiments.

METHOD DETAILS

Generation of Stable Cell Lines

Seipin KO Cells

Generation of 431 Seipin KO cells has been described (Salo et al., 2016). Briefly, A431 cells were co-transfected with Cas9 nickase and two matching pairs of sgRNA expressing plasmids and placed under puromycin selection for 48 h after transfection, followed by culturing in medium without selection for 4 days. Single clones were isolated by limiting dilution and identified by PCR-PAGE and lipid droplet phenotype. sgRNAs are described in (Salo et al., 2016), the clone used in this study (Figure S2F) corresponds to Seipin KO S2AB-15 in (Salo et al., 2016).

Generation of Seipin Knock-in Cells

Generation of end-seipin-sfGFP cells has been described (Salo et al., 2016). Briefly, sfGFP and a linker (3XGGGGS) were integrated into a homology directed repair template of BSCL2 (seipin), to insert into the genomic locus of seipin C-terminus. Clones were isolated after transient selection with puromycin. Recombination templates and sgRNAs are described in (Salo et al., 2016). SNAPf tag (Sun et al., 2011) (Addgene #58186, a gift from Michael Davidson) and mAID-mEGFP (mAID from Addgene #72825 (Natsume et al., 2016), a gift from Masato Kanemaki, fused with monomeric EGFP), were amplified by PCR and integrated into BSCL2 (seipin) homology directed repair templates to insert at the C-terminus of genomic locus of seipin by CRISPR/Cas9-mediated genome editing (Ran et al., 2013) (Figure S1A). For generation of end-seipin-GFPx7 cells, endogenous seipin was tagged with GFP11x7 (Addgene #70224 (Kamiyama et al., 2016), a gift from Bo Huang), which only becomes fluorescent after self-complementation with a non-fluorescent GFP1-10 fragment expressed in the same cell (Kamiyama et al., 2016). We adopted the co-selection strategy to simultaneously tag endogenous seipin and integrate the cassette overexpressing GFP1-10 into the well-defined AAVS1/Safe Harbor locus through homology directed repair. Briefly, 3 plasmids (plasmid 1: Seipin-GFP11x7 homology directed repair template; plasmid 2: the GFP1-10 overexpression cassette together with puromycin selection marker on AAVS1 integration template; plasmid 3: Cas9, sgBSCL2/seipin, sgAAVS1 overexpression plasmid) at 5:1:4 ratio were transfected into A431 cells. Cells were selected with puromycin and single clones were isolated by limiting dilution. Of note, GFP1-10 fragment was codon-optimized and synthesized by

Genescript, as the plasmid (Addgene #70219 (Kamiyama et al., 2016) a gift from Bo Huang) was of low codon adaption index (CAI, analysed at www.genscript.com/tools/rare-codon-analysis) and was poorly expressed in human cells in our hands. For all end-seipin cell lines, single clones were selected based on GFP/SNAP-label fluorescence and homozygous knock-in validated by genomic PCR and western blot with in-house generated seipin antibody and antibodies against the tags (SNAP and GFP).

Generation of Rab18 and ACSL3 Knock-in Cells

sfGFP (Addgene #56482 a gift from Michael Davidson) was amplified by PCR and integrated into the homology directed repair templates of ACSL3 and Rab18 to insert into the genomic locus of ACSL3 C-terminus and Rab18 N-terminus. Recombination templates and sgRNAs are described in Figures S1E and S4A. Single clones were selected by GFP fluorescence and homozygous knock-in validated by western blot against endogenous proteins.

Generation of seipin NE-trap cells

GFP nanobody-3XFlag-KASH2 (GFP nanobody from Addgene #79649 (Stanley et al., 2016), a gift from Jeffrey Friedman, KASH2 is aa. 6821-6885 of GenPept: NP_055995.4, plasmid with puromycin selection marker and BFP-KDEL) and SUN2 (GenBank: NM_001199580.1 from A431 cDNA, plasmid with blasticidin selection marker) were integrated into AAVS1/Safe Harbor locus through CRISPR/Cas9-mediated genome editing (Ran et al., 2013). Briefly, endogenous mEGFP tagged seipin (end-seipin-mAID-mEGFP) cells were transfected with 3 plasmids (plasmid 1: GFP nanobody-3XFlag-KASH2 overexpression cassette on AAVS1 integration template; plasmid 2: SUN2 overexpression cassette on AAVS1 integration template; plasmid 3: Cas9, sgAAVS1 overexpression plasmid, sgAAVS1 target sequence: GTCACCAATCCTGTCCCTAG TGG) at 3:3:4 ratio. After 24 h, cells were selected with puromycin and blasticidin for 8 days, single clones were isolated through limiting dilution and single clones were selected using GFP fluorescence at the NE as a marker for NE-trapping of seipin. For experiments comparing LD formation at the NE, end-seipin-mAID-mEGFP cells with stable BFP-KDEL expression were used as a control cell line. For the data in in Figure 2B (transiently transfected cells) and Figure S1J (stable expression), end-seipin-sfGFP cells were transfected with GFP nanobody-3XFlag-KASH2 (with puromycin selection marker) and SUN2 (with G418 selection marker) plasmids for random integration. Stable cells were selected with G418 and puromycin and single clones isolated by limiting dilution. With this latter method trapping, less seipins could be trapped at the NE and this varied more from cell to cell. Therefore, for the majority of experiments an AAVS1/Safe Harbor clone was used.

Generation of Seipin Degron Cells

Seipin degron clones were generated on top of end-seipin-mAID-mEGFP cells through introduction of a modified version of OsTIR1 into the AAVS1/Safe Harbor locus through CIRSPR/Cas9 mediated genome editing. OsTIR1 was from Addgene# 72835 (Natsume et al., 2016), a gift from Masato Kanemaki. For seipin degron-A, FAK NES2 sequence followed by a linker and OsTIR1(aa.2-575) was used (amino acids: M**LDLASILIS**G-OsTIR1, bolded amino acids indicate FAK NES2 sequence). For seipin degron-B, OsTIR1(aa.1-575) followed by NES21 sequence (Niopek et al., 2016) was used (amino acids: OsTIR1-IDELLKELADLNLD) was used. Single clones were isolated by limiting dilution and seipin depletion upon IAA addition was validated by western blotting. End-seipin-mAID-mEGFP cells, which do not express OsTIR1, were used as controls.

Generation of Rab18 KO Cells

Rab18 KO was done similarly as described (Salo et al., 2016). Briefly, sgRAB18 (target: tcctcatcatcggcgagagt ggg) was used in combination with Cas9 plasmid containing Zeocin selection marker. Seipin degron-B cells were transfected, and 24 h later selected with Zeocin for 2 days, followed by culturing in medium without selection for 4 days. Single clones were isolated by limiting dilution and Rab18 KO clones identified by western blot using anti-Rab18 antibody.

Introduction of Exogenous Fluorescence Markers into Genome-Edited Cell Lines

LiveDrop-mCherry was a gift from Robert. V. Farese (Wang et al., 2016), BFP-KDEL (Addgene #49150) was a gift from Gia Voeltz (Friedman et al., 2011). Indicated genome-edited cell lines were transfected and stable pools were selected with G418 and, in the case of LiveDrop-mCherry + BFP-KDEL cells, sorted by FACS with BD Influx Flow Cytometer (BD Biosciences, USA) at HiLIFE Biomedicum Flow cytometry unit, University of Helsinki to enrich a pool of highly co-expressing cells prior to single cloning. Single clones were isolated by limiting dilution.

siRNAs and Lentiviruses

Ctrl and seipin siRNAs have been described (Hölttä-Vuori et al., 2013). siRNAs against ACSL3 have been described (Salo et al., 2016), siRNAs against TIP47/PLIN3 have been described (Gangley et al., 2005). siRNAs against SUN2 and SUN1 were from Ambion (SUN1 Ambion siRNA ID:s23630; SUN2-1 Ambion siRNA ID: s24466 and SUN2-2 Ambion siRNA ID: s24465). Pre-validated Rab18 siRNA sequence was from Qiagen. FITM2 siRNA was from Ambion (s43312). ATGL siRNA was from Ambion (s32683). Lentivirus expressing shBSCL2 was from Sigma (Mission shRNA) and was packaged at Functional Genomics Unit, University of Helsinki, and titers determined by p24 capsid protein concentration. Lentivirus transduction (5 MOI) was performed in the presence of polybrene. Experiments were conducted >14 days after transduction.

Lipid Analyses

LD Isolation

LDs were isolated essentially as previously described (Pfisterer et al., 2017). Briefly, cells were washed with cold PBS and resuspended in 3.5 ml hypotonic lysis buffer (HLM; 20mM Tris pH 7.4, 1 mM EDTA), and incubated on ice for 10 min. Cells were disrupted by repetitive passaging through a 25 g needle, 3 ml of cell suspension was transferred to a Beckmann polyallomer tube (No. 331374) and mixed with 1.5 ml 60% sucrose solution, overlaid gently with 4 ml 5% sucrose solution and 4 ml HLM buffer. Samples were

centrifuged at 100 000 g with a SW40 rotor for 90 min, at +4°C, no brakes. The top 1.2 ml was collected as LD fraction, and the bottom pellet was resuspended in HML buffer and designated as membrane fraction. All steps were performed on ice. For imaging of isolated LDs (Figure S3B), freshly isolated LDs in HML buffer were placed onto to a coverglass, which was sealed with Gene Frame double sided tape and overlaid with a High performance thickness no. $1^{1/2}$ cover glass. The fractions were immediately imaged with Nikon Eclipse Ti-E microscope, 100X PlanApo VC oil objective NA 1.4 with 1.5x zoom at RT, acquiring 0.3 μm z-stacks. Z-stacks were deconvolved using Huygens.

Lipid Extraction, Mass Spectrometry

For analysis of neutral lipid contents from cells (Figure 4D), lipid extraction and HPTLC were performed as described (Salo et al., 2016), based on Bligh-Dyer lipid extraction (Bligh and Dyer, 1959). Briefly, cells were scraped into PBS, and equivalent protein amounts (measured by DC protein assay) were adjusted to 800 μl of PBS in a glass tube. 1 ml of chloroform and 2 ml of methanol was added, samples were vortexed and proteins pelleted by centrifugation at 725 g for 10 min at +4°C. The supernatants were then transferred to new glass tubes, and 1 ml of chloroform and 1 ml of 0.01% acetic-acid-mqH_20 was added. Samples were thoroughly mixed, vortexed and centrifuged at 725 g for 10 min at + 4°C. The upper (organic) phase was transferred to a new tube, and the solvent evaporated under nitrogen flow at 42°C. The resulting lipid film was resuspended into 100 μl of chloroform:methanol 9:1. 80 μl of the samples were applied to high performance TLC silica plates by Camaq Automatic TLC sampler 4 (Camaq) and developed in hexane/diethyl ether/acetic acid (80:20:1) as the solvent. Lipids were visualized by dipping the plate into $CuSO_4$(3%)/H_3PO_4(8%) and heating for ~5 min at 180° C, the plate was imaged, and the amount of lipid analyzed by densitometric scanning using ImageJ FIJI.

For the analysis of BPY-C12 incorporation into cellular lipids (Figure S5C), lipids were extracted from membrane pellets and isolated LD fractions as described above and run on standard silica gel plates using a two-solvent system (Thiele et al., 2012): the plates were first developed in chloroform:methanol:mq$H_2$0:acetic acid (65:25:4:1) for ~11 cm, dried and developed again for ~19 cm in hexane:ethyl acetate (1:1). Cold lipids were visualized as described above and the BPY signal by imaging with a FLA-9000 imager. The amounts of lipids were analyzed by densitometric scanning using ImageJ FIJI.

Lipid extraction of isolated LDs for mass spectrometry was performed using the acidic Folch method. After partitioning the lower phase was washed once with the Folch theoretical upper phase and dried under nitrogen flow. The lipid film was dissolved in 1 ml of chloroform/methanol (95:5) + 5 μl of 0.5 M HCl and then 50 μl of trimethylsilyldiazomethane (2 M in hexane) was added and the samples were incubated for 10 min at room temperature (RT) in order to methylate the phospholipids (Cai et al., 2016). 6 μl of acetic acid was added to quench the remaining methylation reagent. The lipids were then re-extracted as above but without acidification, dried and dissolved in 40 μl of methanol, analyzed in a LC-MS system consisting of Waters Acquity H-class UPLC and Micro Premier triple quadrupole mass spectrometer. The column (Acquity BEH C4, 1x100 mm, 1.7 μm particle size) was eluted with a gradient of 75% solvent A (acetonitrile/water/5 mM NH_4-formate) to 100 % solvent B (acetonitrile/methanol/5 mM NH_4-formate) in 10 min. This solvent composition was maintained for 5 min and then returned to the initial one and maintained there for 5 min. Glycerophospholipids were detected using class specific neutral-loss scanning in the positive mode (Cai et al., 2016). The neutral losses used were: 198 (PC); 155 (PE); 213 (PS); 291 (PI); 203 (PG). Mass spectrum was then extracted from the chromatograms and the individual lipid species quantified with the LIMSA software (Haimi et al., 2006) using the following internal standards: PC-40:2, PE-40:2, PS-28:2, PI-32:2 and PG-40:2. DAGs were detected using multiple reaction monitoring and quantified QuanLynx software (Waters) using DAG-40:2 as the internal standard.

Click-Labeling

For click-labeling experiments (Figure 4C), cells were first treated with IAA and OA as indicated. Cells were then incubated with 200 μM alkyne-oleate (1mM stock complexed with BSA in 8:1 molar ratio prepared in serum-free DMEM as described (Hölttä-Vuori et al., 2013)) in serum free medium for 10 min, washed with 1% BSA/PBS, and incubated with 200 μM OA for 20 min (chase). Cells were then collected, LDs and membrane fractions isolated and lipids extracted as described above. The lipid extracts were then reacted with 3-azido-7-hydroxycoumarin in the presence of Cu(I) as described in detail in (Thiele et al., 2012). After the click reaction, products were separated on standard silica gel TLC plates using the two-solvent system described above, and the plates were developed and imaged as described in detail in (Thiele et al., 2012). Densitometric analysis of the fraction of alkyne-OA incorporated into cellular lipids was analyzed from images as percentage of total lane intensity with ImageJ FIJI.

Antibody Generation and Immunoblotting

Seipin Antibody Generation

The coding region of the C-terminal region of human seipin (amino acids 278-394 of NM_001122955.3) was amplified from human cDNA by PCR and cloned into the pGEX-2T expression vector (GE Healthcare). The GST-Seipin fusion protein was expressed in BL21(DE3) cells, and purified by glutathionine sepharose (according to the manufacturer, GE Healthcare). The protein was used for immunization of three rabbits (Pineda, Antikörper-Service, Berlin, Germany). The antisera were affinity purified by using GST-Seipin linked to Affi-10-Gel^R according to the manufacturer (Bio-Rad). The specificity of the affinity purified antibody was tested by immunofluorescence and western blotting (1:400-1:500 dilution) using seipin knockout and seipin overexpressing cells.

Immunoblotting

Cells were lysed in buffer containing 1.0% Igepal CA-630, 0.05-0.5% sodium deoxycholate, 0.1% sodium dodecyl sulfate, 250 mM Tris-HCl, pH. 7.5 and 150 mM NaCl with protease inhibitors. Equal amounts of protein were loaded onto 10% or 12% Mini-Protean TGX Stain-Free gels and transferred onto nitrocellulose membrane. Membranes were blocked with 5% milk in TBS containing 0.1% Tween-20 for 1 h at RT, and subsequently probed with primary antibodies at +4°C overnight. After washing with TBS containing 0.1%

Tween-20, membranes were incubated with secondary antibodies for 1 h at RT. Membranes were washed, incubated with ECL or ECL Clarity Max substrate, and imaged with a ChemiDoc Imaging System (Bio-Rad). Band intensities were quantified in ImageJ FIJI and normalized to total protein content quantified with the Stain-Free technology (Bio-Rad). Stain-Free total protein signals from the same region as the band of interest are shown as loading controls in the figures. Antibody dilutions are indicated in the Key Resources Table.

Light Microscopy and Image Analysis

Live and Fixed Cell Imaging

Cells were seeded onto Ibidi μ-slide 8 well ibiTreat chambers for widefield microscopy; or 8-well Lab-Tek II #1.5 coverglass slides for Airyscan microscopy and FRAP experiments, the latter coated with 10 μg/ml fibronectin. Similar coating was also used for CLEM experiments. All live cell imaging experiments were performed at +37°C, 5% CO_2 in FluroBrite DMEM supplemented with 10% FBS or 5% LPDS. For all live cell Airyscan imaging, ProLong Live Antifade was used during imaging. For light microscopy of fixed cells, cells were washed with PBS, fixed with 4% PFA in 250 mM Hepes, pH 7.4, 100 μM $CaCl_2$ and 100 μM $MgCl_2$ for 20 min, followed by quenching in 50 mM NH_4Cl for 10 min and 3 washes with PBS. For immunofluorescence staining, cells were subsequently permeabilized with 0.1% saponin in PBS for 10 min at RT, and then blocked by incubation with 10% FBS in PBS for 30 min at RT. Primary (2 h) and secondary (1 h) antibody incubations were done in 10% FBS in PBS at RT, with three 5 min PBS washes in between. The final wash solution prior to each antibody incubation also contained 0.1% saponin. LD dyes and DAPI were diluted in PBS. Antibody and dye dilutions are indicated in the Key Resources Table.

Image Processing

Airyscan images and videos were Airyscan-processed using the Zeiss Zen software package with identical (default) settings for all acquisitions. Deconvolution, where indicated, was performed in Huygens software (Scientific Volume Imaging) using iterative Classic Maximum Likelihood Estimation. Brightness, contrast and scale bars were adjusted in ImageJ FIJI and Corel Draw 2017 (64 bit).

Live Cell Widefield Imaging and Analysis

Cells were imaged with Nikon Eclipse Ti-E microscope equipped with 100x Plan Apo VC oil objective, Nikon Perfect Focus System 3, Hamamatsu Flash 4.0 V2 scientific CMOS and Okolab stage top incubator system. For data in Figures 4A and 4B, seipin degron ctrl cells expressing BFP-KDEL and seipin degron-A cells were co-plated 1 day prior, and treated with OA for 2 h prior to imaging. Cells were then transferred into FluroBrite medium containing 10% FBS, OA, LD540 and IAA, and focus was set on the cellular plane below the nucleus, where LDs are relatively immobile in the z-plane. BFP-KDEL signal was imaged once to map ctrl cells from degron cells, and time lapse imaging was started, imaging every 25 min for 8 h. Only LD540 signal was recorded with minimal light settings and exposure times to minimize phototoxicity. Analysis of LD size changes was performed in Image J FIJI. Nearby LDs that could be reliably followed for at least 2 h were selected and their size changes measured manually. BFP-KDEL signal was then used to discern whether these LDs were in degron ctrl or seipin degron cells.

Fixed and Live Cell Airyscan Imaging

Cells were imaged with Zeiss LSM 880 confocal microscope equipped with Airyscan (Fast) detector using a 63 × Plan-Apochromat oil objective, NA 1.4. After fixing, cells were kept in PBS until imaging and stained for LDs immediately prior to imaging. Imaging was done within 48 h after fixing, using super resolution mode. The Airyscan detector was adjusted regularly between acquisitions. Live cell imaging was performed at 37°C, 5% CO_2 with incubator insert PM S1 and definite focus hardware autofocus system. Images were Airyscan processed automatically using the Zeiss Zen software package. Live cell imaging was done in Airyscan super resolution ILEX-mode (Figures 1H and 7H) or super resolution fast mode (Figures 1A, 1E, and 1F), with sequential excitation of fluorophores using appropriate lasers and stable emission filter sets. With this imaging regime cross talk between signals was minimal, and singly labeled specimens were used as controls. The Airyscan detector was adjusted regularly between time-lapse acquisitions.

For live cell data in Figures 1A–1H, single focal planes were imaged with Airyscan fast mode, with frame rates of 650 ms (Figures 1A, 1E, and 1F) or 10 s (Figure 1H). A cell of interest showing well defined ER-elements at the relatively flat plane of the ER below the nucleus was selected. OA in FluoroBrite containing 5% LPDS was added to cells and imaging was started 50 s later. For the data in Figure 1G, analysis was done in ImageJ FIJI. First, the end-seipin-GFPx7 channel was bleach corrected using Histogram matching. Then seipins were tracked manually and the background corrected intensity of LiveDrop and BFP-KDEL measured at a circular ROI of 0.142 μm^2 with the seipin spot in the center. This was done for each individual frame for each tracked seipin spot, and the ratio of LiveDrop/KDEL signal at that spot vs ratio of LiveDrop/KDEL signal in ER regions where no LDs were forming was used to plot the graph in Figure 1G. Motility of seipins was calculated by the displacement of the ROIs between frames. Seipins were considered LD forming if they showed LiveDrop accumulation at the end of the recording (~4 min after OA). For the data in Figures 7G–7I, seipin degron-A cells stably expressing BFP-KDEL were co-plated with end-seipin-GFPx7 cells. After 2 days delipidation, cells were fused with PEG1500 for 1 min, followed by 4 washes with PBS as in (Salo et al., 2016). 1 h later, medium was changed to DMEM containing 10% FBS and OA for 2 h. Then medium was changed to FluroBrite containing 10% FBS, OA, IAA and LipidTox Deep Red and cells were transferred to the microscope. Cells were selected based on the criterion that they should contain an ER network stained by BFP-KDEL signal (originating from degron cells) and bright seipins (originating from seipin-GFPx7 cells). Z-stacks covering the whole bottom region of the ER network below the nucleus were acquired of the GFP and LipidTox signal every 15 min. For analysis, nearby LDs (one containing seipin and one without), which were trackable for at least 60 min were selected. Analysis of LD size changes was performed in Image J FIJI.

BPY-C12 FRAP

Cells were imaged with a Zeiss LSM 880 confocal microscope, using a 63 × Plan-Apochromat oil objective, NA 1.4. Cells were labeled with 1 μM BPY-C12 for 4.5 h in the presence of 200 μM unlabeled OA. Cells were then washed 3 times with PBS and transferred to FluroBrite DMEM, containing 10% FBS, LipidTox Green and IAA, but without BPY-C12. FRAP was performed 45-120 min later, acquiring images of both LipidTox Green and BPY channels simultaneously. After 10 pre-bleach acquisitions with 1 s intervals, bleaching of BPY-signal at LD pairs and LD clusters in a circular ROI of 26.2 μm^2 was done using 514 and 560 nm lasers at 100% power. Recovery was followed for 110 s at 1 s intervals. For analysis, performed in Image J FIJI, the intensity in the BPY channel of each bleached LD was measured for the duration of acquisition and corrected for BPY signal in a non-bleached, non-LD containing region of the cell. LipidTox Green signal was used to track the LDs. For each LD, the total recovery was calculated as the fraction of BPY recovered during the whole acquisition (measured by averaging the BPY intensity of the LD during the 5 final frames of the acquisition), normalized to background corrected pre- and –post bleach intensities. The difference of recovery between adjacent LDs in same ROI was calculated as described in Figure S5D. To ascertain equivalent BPY-C12 labeling and conditions for the cells, for the data in Figures 4F–4I, S5F, and S5G, degron ctrl cells stably expressing BFP-KDEL and degron-A cells were co-plated. During the experiment, the BFP-KDEL channel was used to identify cells belonging to each population. BPY-C12 FRAP of primary human fibroblasts (Figure S5H) was performed as described above, with a bleached ROI of 1.6 μm^2, and BPY recovery to LDs was followed for 200 s at 2 s intervals.

Fixed Cells Widefield Imaging and LD Size Analysis

Analysis of LD size distributions in cells was based on a previously described protocol (Pfisterer et al., 2017). Cells were grown on Ibidi 8 μm dishes, fixed, quenched and stained with LD540 (LDs) and DAPI (nuclei). For some experiments also CellTracker Red (cytoplasm) was utilized, this labeling was performed in live cells 30 min prior to fixing. Z-stacks spanning the whole cell (step size 0.3 μm) were acquired with Nikon Eclipse Ti-E microscope, 60X PlanApo VC oil objective NA with 1.5x zoom, and image stacks were automatically deconvolved using the Huygens batch processing application, and deconvolved image stacks were maximum intensity projected by custom MATLAB scripts. Cell segmentation and LD detection was performed with CellProfiler (Carpenter et al., 2006) in a hierarchical manner. First, cell nuclei were detected in DAPI images based on the Otsu adaptive thresholding method. Touching nuclei were separated by built in intensity methods. Second, the cytoplasm was detected by utilizing the faint cellular background of DAPI channel or CellTracker Red labeling, using intensity propagation based on the Otsu adaptive thresholding method using the identified nuclei from the first step as a seed point. To detect LDs, a CellProfiler module was generated called DetectAllDroplets. The module performs multi-level A-trous wavelet transform to identify spot centroids, static/Otsu threshold is applied combined with propagation to segment the LDs on each A-trous level. Additionally, an extra layer is defined to search for the largest LDs with Hough-transform. Then the overlapping LDs from each level are merged into a single-layer segmentation such that the LDs with higher circularity are preserved. Finally, to prune the segmentation, the UnifyObjects module was used to merge LDs close to each other showing homogeneous intensity profile on the LD540 channel between their centroids. Feature analysis, including LD size distributions, mean and total LD areas/cell, number and area of LDs overlapping with nucleus and closest contour distances between droplets was done with a custom Matlab software generated for post-processing.

Analysis of Nascent LDs and Seipin Association in Fixed Cells

For analysis of nascent LDs and seipin association from Airyscan images (Figures S1F, 7B, 7C, and S7D), LDs and seipins were first segmented with ilastik (Sommer et al., 2011)), utilizing machine learning algorithms. Downstream batch analysis was performed in CellProfiler extended with MATLAB code generated for post-processing analysis. LDs were considered seipin-associated if the contour of the segmented LD overlapped with the contour of the segmented seipins. For analysis of LDs in Airyscan images of NE-trapped cells (Figures 7E and 7F), LDs were first detected with ICY software (de Chaumont et al., 2012) and downstream batch analysis was performed in CellProfiler extended with custom MATLAB code generated for post-processing analysis.

Analysis of Newly Formed LD Distances to Other LDs

LDs were first thresholded in ImageJ FIJI and ROIs in the NE ER plane cropped. For Figure 1C this entailed LDs that were visible at the end of the timelapse recording, and for Figure S1J this entailed LDs at the bottom nuclear plane in fixed cell images. For each of the segmented LD images, 10 reshuffled images were generated, containing the same number and sized LDs as the original image, but with randomized, non-overlapping positions. This was done using a custom-made ImageJ macro. The nearest contour distance of segmented LDs to its two nearest neighboring LDs was analyzed using CellProfiler, extended with custom MATLAB code, comparing real and simulated data. For Figure S1C the distances of an emerging LD to its two nearest neighbouring LDs (either pre-existing LDs or LDs emerging within a +/- 5 s time window from the LD in question) at the time of the LDs first appearance was measured from live cell videos manually in ImageJ FIJI. For all these analyses, only LDs where the two nearest neighbouring LDs were closer than the edge of the image were considered for analysis.

Electron Microscopy and Analysis

CLEM

Cells were grown on fibronectin coated dishes with gridded glass cover slips (MatTek). For Figures 1I and 1J, cells were fixed with 2% formaldehyde, 1.5% glutaraldehyde in 50 mM HEPES buffer, pH 7.3, supplemented with 2 mM $CaCl_2$ for 25 min at RT. Cells were kept in 50 mM HEPES and imaged by Zeiss LSM880, first using transmission and confocal mode (to identify cell position in relation to markings on the coverglass) and then by Airyscan microscopy (to image end-seipin-GFPx7 and BFP-KDEL signal), using 40X oil objective, NA 1.40 and super resolution mode. After this, samples were kept in 50 mM HEPES, +4°C until subsequent treatments the

following day. For Figure 2G, cells were first fixed with 4% formaldehyde, 0.2% glutaraldehyde in 0.2 M HEPES for 25 min at RT, then immediately imaged in 0.1 M phosphate buffer, pH 7.4, as above. Cells were then fixed again with 2.5% glutaraldehyde in 0.2 M HEPES for 25 min and kept in 0.1 M phosphate buffer, +4°C until subsequent treatments the following day.

After light microscopy, cells were post-fixed with 1% reduced osmium tetroxide in 0.1 M sodium cacodylate buffer, pH 7.4 for 1 h at RT, *en bloc* stained with 1% uranyl acetate in 0.3 M sucrose for 1 h at 4°C, and flat embedded as described previously (Seemann et al., 2000). The target cells were identified according to the finder grid pattern transferred to the block surface, and a pyramid covering the area of interest was trimmed. Serial 230-nm-thick sections parallel to the cover slip were cut with a 35° diamond knife (Diatome, Switzerland) on ultramicrotome (Leica EM Ultracut UC6i or UC7, Leica Mikrosysteme GmbH, Austria) and collected on Pioloform-coated single slot copper grids. The target areas for 3D-imaging were defined by correlating the ER profiles in TEM micrographs and BFP-KDEL signal in fluorescence microscopy images using Corel PHOTO-PAINT. One to three consecutive semi-thick sections having the overlapping signal/features/profiles were subjected to ET.

Electron Tomography

For ET of CLEM samples, cells were first treated as described above. For data in Figures 2E, 2F, S2G, and S2H, cells were fixed with 2-2.5% glutaraldehyde in 0.1 M sodium cacodylate buffer, pH 7.4 containing 2 mM $CaCl_2$ with or without 2% formaldehyde for 30 min at RT. After post-fixing with 1% osmium tetroxide in 0.1 M sodium cacodylate buffer for 1 h at RT, the cells were flat embedded as described previously (Seemann et al., 2000). For ET, the acquisition of dual axis tilt series and reconstructions were done as described (Salo et al., 2016), except using nominal magnification of 11.500x. Segmentation and visualization were done with MIB (Belevich et al., 2016)) and Amira, respectively. For data in Figures S2A and S2B, A431 cells and primary human fibroblasts were fixed and imaged as described (Salo et al., 2016). For visualization, tomograms were denoised using nonlinear anisotrophic diffusion filter, K=1.2 for 11 iterations (Frangakis and Hegerl, 2001). Measurements of membrane-LD contact site parameters were done using ImageJ FIJI and analysis of contact site areas using MIB.

Model Membrane Studies

Incorporation of Artificial Droplets into GUV Membranes to Make DEVs and Model Membrane Imaging

GUVs were prepared with 99.5% DOPC and 0.5% (w/w) Rhodamine-DOPE by electro-formation (Chorlay and Thiam, 2018; Ben M'barek et al., 2017). Phospholipids and their mixtures in chloroform at 0.5 μM were dried on an indium tin oxide (ITO) coated glass plate. The lipid film was desiccated for 1 h. The chamber was sealed with another ITO coated glass plate. The lipids were then rehydrated with a sucrose solution (275 +/-15 mOsm). Electro-formation was performed using 100 Hz AC voltage at 1.0 to 1.4 Vpp and maintained for at least 1 h. GUVs were either stored in the chamber at 4°C overnight or directly collected with a Pasteur pipette. Experiments were performed in the following HKM buffer: 50 mM Hepes, 120 mM Kacetate, and 1 mM MgCl2 (in Milli-Q H_20) at pH 7.4 and 275 +/- 15 mOsm. Preparation of the GUVs embedded with artificial LDs (DEVs): artificial LDs were made by adding 5 μl of the triolein oil phase to 45 μl of HKM buffer and the mixture was sonicated for 1 min. Then GUVs were incubated with the artificially made LDs for 5 min under gentle mixing. The GUV-LD mixture was then placed on a glass coverslip to generate flat membranes embedded with droplets. Alternatively, to have intact DEVs, the glass coverslip was pretreated with 10 % (w/w) BSA. Confocal imaging of DEVs was done with Zeiss LSM 800 microscope, equipped with 10x air and 60x oil objectives and image analysis was done with ImageJ FIJI.

Incorporation of Cellular Lipid Droplets into GUV Membranes to make DEVs and Model Membrane Imaging

GUVs were formed using a gel-assisted method (Weinberger et al., 2013) with slight modification. Briefly, 24 x 24 mm coverslips were cleaned by sonicating sequentially in water, ethanol and acetone for 10 min, then in 1M KOH for 20 min and water for 10 min. The polyvinyl alcohol (PVA)-coated substrates were prepared by spreading 50 μL of 5% (w/w) PVA solution on the clean coverslip, which was dried for 30 min in an oven at 50°C. The lipid mixture DOPC:rhodamine-DOPE (99:1, molar ratio) was dissolved in chloroform (1 mM) and 10 μL lipids were spread on the PVA-coated coverslip and placed under vacuum for 30 min at room temperature. The lipids were then rehydrated in 1 ml swelling buffer (20 mM Tris, pH 7.5, 50 mM NaCl, 20 mM sucrose) in a 35 mm cell culture petri dish, kept stable in dark for 45 min at room temperature and GUVs were collected for experiments. After this, 27 μl of GUVs in swelling buffer were mixed under gentle shaking with 3 μl of isolated cellular LDs labeled with LipidTox Deep Red (1:500 final concentration). The GUV-LD mixture was then placed on a glass coverslip to generate flat membranes embedded with droplets. Z-stacks covering the whole system were imaged by Airyscan or widefield microscopy at 10 min imaging intervals for 3 hours. LDs were segmented with Ilastik and size changes of segmented LDs tracked using ImageJ FIJI.

QUANTIFICATION AND STATISTICAL ANALYSIS

Statistical analysis was performed with Graphpad Prism (Graphpad Software), using statistical tests as indicated in the figure legends. p-values < 0.05 were considered significant.

DATA AND SOFTWARE AVAILABILITY

Custom software scripts (to be used with CellProfiler and MATLAB) for LD size analysis can be found at https://bitbucket.org/szkabel/lipidanalyser/get/master.zip. A detailed description of the tools is reported separately.